Formation and Characterization of Nanobubbles with an Electrochemical Quartz Crystal Microbalance

Doctoral Thesis

(Dissertation)

to be awarded the degree

<Doctor rerum naturalium>

submitted by

Anne Finger

from Frankenberg/Eder

approved by the Faculty of Natural and Materials Sciences,

Clausthal University of Technology

Date of oral examination

07.09.2012

Chairperson of the Board of Examiners:

Prof. Dr. Dieter Kaufmann

Chief Reviewer:

Prof. Dr. Diethelm Johannsmann

Reviewer:

Priv.-Doz. Dr. Jörg Adams

Abstract

Surface attached nanobubbles were produced via electrochemical decomposition of water with aid of a three-electrode setup. During this electrochemical process the interface of the working electrode (WE) was probed by a Quartz Crystal Microbalance (QCM). This combination of a three-electrode setup with a QCM is called Electrochemical Quartz Crystal Microbalance (EQCM). This setup gave information about the changes of the sample's properties on applying a potential.

When stepwise decreasing the potential of the WE, a development of gas bubbles could be observed. For high negative potentials, which correspond to big bubbles, the expected positive frequency shifts were observed. Caused by the lower density of an inhomogeneous liquid-gas sample, relative to pure liquid, the resonance frequency of the quartz crystal was increased. For small negative potentials the observed frequency shifts were *negative*. This effect was not expected, because small bubbles should result in positive frequency shifts as well.

These negative frequency shifts must be caused by an increased mass coupled to the QCM. Bubbles of nanoscopic size exhibit a high internal pressure. The deformation of those, due to oscillation of the crystal, is suppressed. Therefore the bubbles trap the surrounding water in between them and drag the liquid along with the movement of the crystal. This increases the mass coupled to the QCM. The result is a negative frequency shift. The sample does no longer couple to the quartz crystal like a liquid, but like a solid film.

In this thesis the influences on the obtained frequency shifts were examined. The consequences of varying the electrolyte and additives were discussed. This should lead to better understanding of the properties of nanobubbles and the mechanism of their formation.

Zusammenfassung

Nanoblasen wurden durch elektrochemische Zersetzung von Wasser mit einem Drei-Elektroden Aufbau hergestellt. Diese Blasen traten an der Oberfläche der Elektrode auf. Während des elektrochemischen Prozesses wurde die direkte Umgebung der Arbeitselektrode (WE) mit Hilfe einer Quarzmikrowaage (QCM) untersucht. Dieser kombinierte Aufbau aus einem elektrochemischen Aufbau mit einer QCM heißt Elektrochemische Quarzmikrowaage (EQCM). Dieses Messverfahren gab Aufschluss über die Änderung der Eigenschaften der Flüssigkeit an der WE, wenn ein Potential an dieser angelegt war.

Durch eine schrittweise Verringerung des Potentials an der WE konnte die Entwicklung der Gasblasen an der Elektrode beobachtet werden. Bei großen negativen Potentialen, welche zu großen Blasen führen, wurden die erwarteten positiven Frequenzverschiebungen gemessen. Diese werden durch die geringere Dichte der inhomogenen Flüssigkeit/Gas Schicht relativ zur reinen Flüssigkeit hervorgerufen. Für kleine negative Potentiale wurden *negative* Frequenzverschiebungen erhalten. Auch hier wurden positive Frequenzverschiebungen erwartet.

Negative Frequenzverschiebungen können nur durch eine Vergrößerung der zum Quarz gekoppelten Masse hervorgerufen werden. Nanoskopische Blasen besitzen einen hohen Innendruck. Dadurch ist eine Deformation, die durch die Oszillation des Quarzes hervorgerufen wird, unterdrückt. Das umgebende Wasser wird zwischen den Blasen gefangen und mit dem Quarz mitbewegt. Die zur QCM gekoppelte Masse wird so erhöht. Für die QCM erscheint die Probe nicht wie eine Flüssigkeit, sondern wie ein fester Film.

In der vorliegenden Arbeit wurden die Einflussfaktoren auf die Frequenzverschiebungen untersucht. Insbesondere die Änderung des verwendeten Elektrolyten und der Zusatz von Additiven wurden genauer betrachtet. Dies führt zu einem besseren Verständnis der Nanoblasen und dem Mechanismen ihrer Entstehung.

Acknowledgments

I want to thank all the people that helped me to write this thesis. Especially I want to thank Diethelm Johannsmann for supervising me. For the opportunity to work on this topic and a lot of helpful discussions during my whole PhD I am very grateful.

Jörg Adams I want to thank for reviewing this thesis.

For introducing me into all practical aspects of the EQCM I am thankful to Johanna Bünsow. Discussions about results and experiments were provided by Arne Langhoff and Sylvia Hanke. I want to thank Stina Bauer for a lot of help in both practical and theoretical matters.

For vacuum vaporization of the quartz crystal electrodes and various help in the lab I want to thank Judith Petri. The program for controlling the function generator was programmed by Jens Hagge.

For critical reading of this thesis I want to thank Arne Langhoff, Sylvia Hanke, Katja Pohl, Stefanie Telsemeyer-Schauer, Stina Bauer and Jens Hagge.

I want to thank my students Stina Bauer, Karoline Brandenburg, Christopher Ehrhardt, Madita Flamm, Sebastian Klepatz, Matthias Meinecke, Philipp Memmel, and Yi Zhou, who helped me during my PhD thesis in the lab.

Personal thanks go to Nena Christiansen, Svenja Grube, Henrike Rempel, and Eva Vogt. I also want to thank Jens Hagge for the support during the PhD. I am indebted to my parents Hans and Wilma Finger for more than financial support during my studies and afterwards.

Table of Contents

1 Introduction

Bubbles of nanoscopic size attached to a surface gained interest since their first observations. The occurrence of long range hydrophobic interactions was the first indication for the existence of surface nanobubbles.[1] In those measurements the nanobubbles led to bridging between two surfaces. Images of nanobubbles obtained with Atomic Force Microscopy (AFM) followed.[2] The field of nanobubbles is controversially discussed, because the very existence of nanoscopic bubbles is in disagreement with classical theories. Small bubbles should dissolve rapidly due to their high internal pressure. However many report on stable nanobubbles which they observe in experiment.

The most common approach for investigating surface attached nanobubbles is the AFM. This technique leads to images of the observed surface. This is a big advantage. On the other hand problems exist concerning the interactions of cantilever and sample. Those can induce artifacts and wrong sizes of the bubble. Misinterpretation of the data is possible.[3]

Other methods to measure nanobubbles must be adopted to their small size. For this purpose the Quartz Crystal Microbalance (QCM) is a useful tool. It is a well known and widely used surface sensitive sensor.[4] The investigated samples can be of various kinds. Simple homogeneous samples, like thin rigid films, can be analyzed as well as complex systems that are heterogeneous. The QCM also operates in liquids. Therefore it is possible to couple the QCM with an electrochemical setup. The processes at the electrode can be analyzed *in-situ* while applying various potentials. In this work this simple but very sensitive technique was employed to investigate the formed bubbles.

Since nanobubbles are a relatively new subject of research, basic understanding of their properties is necessary. Influences on their formation and properties are important to know and understand. Therefore the main topic of this thesis is on nanobubbles and the response of the QCM on their appearance. Building on a knowledge of formation mechanism, influence factors, and necessary requirements for the evolution of small gaseous domains, it should be possible to produce nanobubbles as desired. Once an

understanding is achieved, various applications can be envisioned, such as templating, cleaning of surfaces, or the manipulation of flow channels to introduce slip.[5]

2 Theory

2.1 Quartz Crystal Microbalance

The Quartz Crystal Microbalance (QCM) is a widely used acoustic sensor.[4, 6, 7] The QCM is applied for the analysis of surface attached polymers,[8, 9] adsorbates,[10, 11] biomolecules,[8, 12] and cells.[13] It is a noninvasive tool to measure interfacial processes *in-situ*. The utilization as a biosensor, in particular, is widely studied.[14] With the QCM it is possible to measure mechanical and viscous properties of the adjacent media.[15] The most common application of the technique is the determination of film thicknesses in the range of a few nanometers.[4, 6]

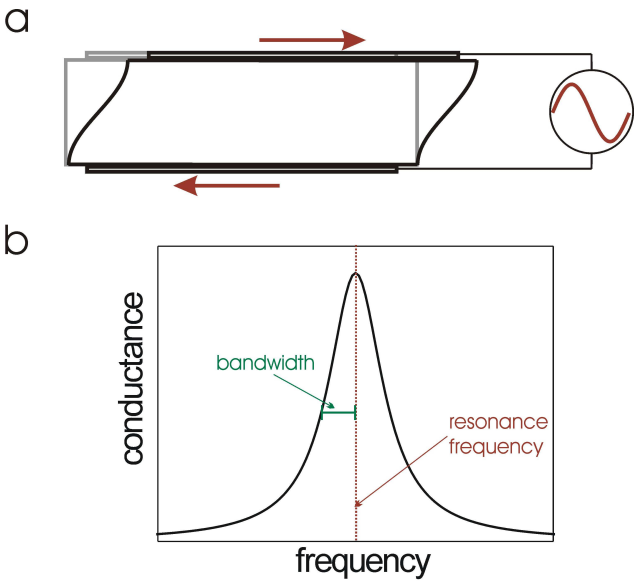

Figure 1: Schematic illustration of a QCM **a**: Oscillation of the crystal excited by an alternating voltage (black), undeformed quartz (grey); **b**: frequency-dependent apparent electrical conductance of the quartz around the resonance frequency. The maximum of the apparent electrical conductance is at the resonance frequency of the QCM and bandwidth refers to the half-width at half-maximum.

The QCM consists of a crystal with piezoelectric properties, usually α-quartz.[16] When a crystal structure has no inversion center, like quartz, piezoelectricity can be found. By deforming the quartz, an electrical polarization develops in between the surfaces of the crystal. This works vice versa as well. When an alternating voltage is applied to electrodes sitting at the front and the back of the crystal a periodic deformation of the crystal occurs (Figure 1a). This deformation is of the thickness-shear type for the

QCM, but it can be of another kind as well. Examples are the torsional deformation or surface acoustic waves.[4a, 6a, 12] When the resonance frequency of the quartz is attained, the apparent electrical conductance shows a maximum (Figure 1b). The resonance frequency is typically in the MHz regime for the QCM. Not only can the frequency of the oscillation at the resonance frequency be obtained, but also the half-width at half-maximum, short "bandwidth".

By deposition of a sample on the QCM the resonance frequency and the bandwidth are shifted. This is caused by the coupling of the sample with the tangential oscillation of the quartz. The nature of these shifts depends on the properties of the sample.

The most common sample on the QCM is a rigid film. This was first studied by Sauerbrey in the 1950s.[17] He found that the shift in frequency, Δf, is proportional to the negative mass of the film per unit area m_f.

$$\Delta f = -m_f \frac{2n \cdot f_F^2}{Z_q} \tag{1}$$

where f_F is the fundamental frequency, Z_q is the acoustic impedance of the quartz ($8.84 \cdot 10^6$ kg·m^{-2}·s^{-1}), and n is the overtone order. The frequency shift induced by the

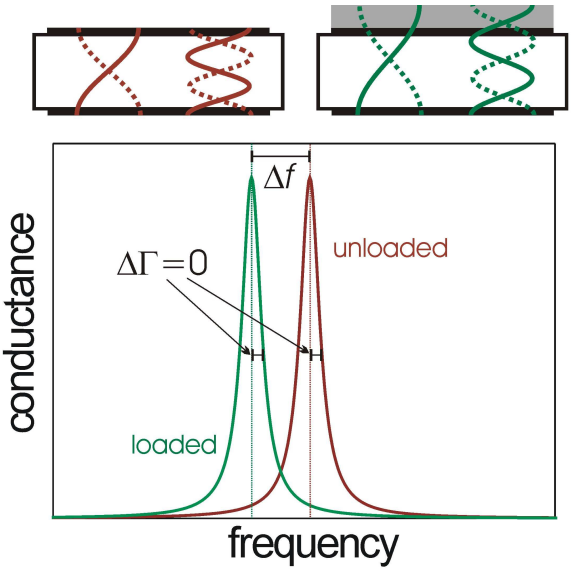

Figure 2: Oscillation of the quartz for first and third harmonic with corresponding conductance spectra. Quartz without a loading (red) and loaded with a rigid film (Sauerbrey loading, green). Frequency and bandwidth shift Δf and $\Delta\Gamma$ gained from impedance analysis. Δf is negative and $\Delta\Gamma$ is zero for Sauerbrey loadings.

rigid film is proportional to the overtone order *n*. For a Sauerbrey loading Δ*f*, divided by the overtone order, must be constant for different overtones. It ought to be noted that for Sauerbrey films the shift in bandwidth ΔΓ is zero (Figure 2). The Sauerbrey equation (1) is valid as long as there is no internal friction and if the added mass couples perfectly with the motion of the QCM.[18] With the Sauerbrey equation (1) the deposited mass on the crystal can be calculated. With knowledge of the density ρ_f of the sample a film thickness Δ*d* can be easily obtained:

$$\Delta d = -\frac{Z_q \cdot \Delta f}{2n \cdot f_F^2 \cdot \rho_f} \tag{2}$$

The Sauerbrey thickness is not the geometrical thickness of the sample.[4, 15] First it must be considered that the quartz crystal averages over its area. Therefore inhomogeneities of the film are not regarded within the measurement and analysis. Secondly, most of the studied samples are not rigid like the metals Sauerbrey used,[17] they behave viscoelastic. Viscoeleastic samples entail a shift in bandwidth. This is caused by dissipation of energy. Only for very thin films, when film thickness is much smaller than the wavelength of sound, the Sauerbrey equation is used as an approximation even if the films are viscoelastic.[19]

Since the mid 1980s the QCM could be also used in liquids.[20-22] The application in liquids gave rise to biosensors[14] and monitoring electrochemical reactions.[9, 23] Caused by the viscous properties of liquids, the oscillation of the crystal is damped. The shear wave decays in the viscous media. This is not the case for a rigid film that is governed by its inertia. The resulting shift in frequency Δ*f* depends on viscosity η_L and density ρ_L of the adjacent liquid.[21]

$$\Delta f = -\sqrt{\eta_L \cdot \rho_L} \cdot \frac{\sqrt{n \cdot f_F^3}}{\sqrt{\pi} \cdot Z_q} \tag{3}$$

The frequency shift scales with the square root of the overtone order *n*. Induced by viscous behaviour dissipation of energy takes place and a bandwidth shift ΔΓ occurs.

$$\Delta\Gamma = \sqrt{\eta_L \cdot \rho_L} \cdot \frac{\sqrt{n \cdot f_F^3}}{\sqrt{\pi} \cdot Z_q} \tag{4}$$

Newtonian liquids should entail shifts of frequency and bandwidth according to Kanazawa (eq. 3 and 4).[21] The characteristic signature for this behaviour are $\Delta f = -\Delta\Gamma$ and $\Delta f \propto \sqrt{n}$.

The propagation of the shear wave in a liquid is quantified by the decay length δ. The sensitivity of the QCM is limited to a range with a thickness of about δ/2.[4b] For a 5 MHz AT-cut quartz crystal, which was used in these studies, δ in water is about 250 nm.[21] This leads to an effective layer oscillating with the crystal, hence QCM is a surface sensitive method in liquids, too.

The frequency and bandwidth shifts determined by the Kanazawa equation (3 and 4) are relative to air. It is likewise possible to choose the liquid as the reference state. Only frequency shifts are detected that are caused by additional changes in the proximity of the crystal (Figure 3).

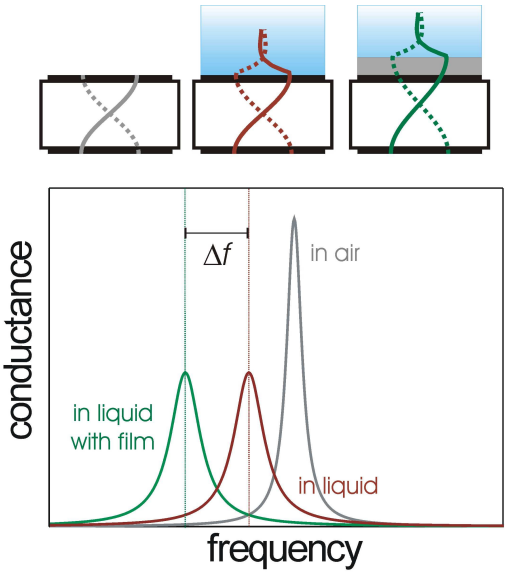

Figure 3: Frequency shift of QCM in liquid with and without a Sauerbrey film. Top: displacement of the first overtone in air, with decaying shear wave in adjacent liquid, and in a liquid with a rigid film. Bottom: conductance spectra and resulting frequency shift for the three systems.

Due to application of a viscoelastic film onto the surface of the crystal, a modification of the Sauerbrey equation results:[4c]

$$\Delta f = -m_f \cdot \frac{2n \cdot f_F^2}{Z_q}\left[\left(1-\frac{\eta_L}{\eta_f}\right)+\left(\frac{\rho_f}{\rho_L}-1\right)\right] \qquad (5)$$

The frequency shift is governed by the ratio of the viscosities of the liquid η_L and the film η_f, as well as by the ratio of the densities ρ_L and ρ_f. By assuming equal densities of film and liquid the sign of frequency shift depends on the ratio of viscosities. If the applied film is more viscous than the liquid ($\eta_f > \eta_L$), a negative frequency shift will be observed. A film with a lower viscosity ($\eta_f < \eta_L$) entails positive frequency shifts.

A more general approach for the mathematical expression of the frequency shift of the QCM induced by a deposited sample is the Small Load Approximation (SLA, Equation 6).[15, 24] The SLA is applicable to most loadings, the only requirement being that $\Delta f << f$. The SLA takes into account that the frequency shift of the QCM may not be caused by a mass of the sample. Very generally, a shift in frequency is proportional to the ratio of shear stress σ and velocity $\dot{u}$ at the surface. This ratio is called load impedance Z_L (equation 7). It is possible to calculate Δf by knowing the load impedance.

$$\Delta f + i\Delta\Gamma = \frac{i \cdot f_F}{\pi \cdot Z_q} \cdot Z_L \tag{6}$$

with

$$Z_L = \frac{\sigma}{\dot{u}} \tag{7}$$

Note that eq. 6 is complex. The left hand side shows the complex frequency shift. Z_L on the right hand side is complex because σ and $\dot{u}$ are complex amplitudes. While for homogeneous loads the determination of Z_L is possible with the theory of planar acoustic multilayers,[24] for heterogeneous systems the load impedance will usually be determined by nummerical means, an example being the Finite Element Method (FEM, see chapter 6). The shear stress for a heterogeneous load is heterogeneous, as well. Importantly, the QCM responds according to the *area-averaged* stress $\langle \sigma_{area} \rangle$ at the interface.

The QCM can measure the frequency and bandwidth shifts in different read-out modes. The most common ones are oscillators,[4d, 25] impedance analysis,[4d, 26] and ring-down method also known as QCM-D.[4d, 27] For the first method the quartz crystal is part of an oscillator circuit and its resonance frequency is ascertained. Oscillators are simple setups which have the big advantage of low cost. When the investigated systems are complex, the other modes are preferred. Oscillators cannot measure on different

overtones hence the dependence of Δf on n is not available. The ring-down technique utilizes the damped oscillation that occurs after the excitation with an impulse. This damped oscillation provides direct excess to Δf and the change in dissipation ΔD. The dissipation is proportional to the bandwidth ($D = 2\Gamma/f$). For all the measurements in this thesis impedance analysis was employed. Spectra, like the one shown in Figure 1, are obtained. A fit of a Lorentzian to the resonance peak leads to Δf and $\Delta\Gamma$.

2.1.1 Electrochemical Quartz Crystal Microbalance

The QCM operates in liquids. Therefore it can be used for monitoring electrochemical reactions.[9, 22, 23, 28] The QCM is a noninvasive method to measure properties of a surface attached film thus it is beneficial to use this technique as an Electrochemical Quartz Crystal Microbalance (EQCM). For this purpose the crystal is incorporated into an electrochemical setup, which can be composed of two or three electrodes. The examined reactions must take place at the front electrode of QCM. For this reason the front electrode generally functions as working electrode.

For the sake of interpreting EQCM data, the reference state and overtone dependence is crucial. Changes of electrolyte can lead to frequency shifts according to Kanazawa (equation 3) due to variation of viscosity or density. The overtone dependence enables to draw conclusions about the nature of deposits at the electrode. Checking for Sauerbrey scaling ($\Delta f \propto n$) or Kanazawa scaling ($\Delta f \propto \sqrt{n}$) yields information about the viscoelastic properties of the sample. Especially swollen films exhibit frequency shifts which indicate too high adsorbed masses. Such an adsorbate does neither develop an overtone dependence according to Sauerbrey nor to Kanazawa, but something in between.

2.2 Potentiostatic Measurement

Electrochemical reactions can be conducted with setups consisting of two or three electrodes. The two-electrode setup seems sensible, because basically electrochemical reactions need just a cathode and an anode. Yet the drawback is that by applying a voltage to the system, the resulting current has an influence on the electrochemical potential and the cell resistance.[29] Therefore voltage and current are coupled and control is hard to achieve.

To ensure control and to obtain information about reactions at the electrode, it is necessary to use a three-electrode setup.[29, 30a] The monitored reaction takes place at the working electrode (WE). With aid of a potentiostat a voltage is imposed between WE and a reference electrode (RE). The reference should be an electrode with a known electrochemical potential, like saturated calomel electrode (SCE) or silver chloride electrode. The setting of the desired potential results in a current in between WE and a counter electrode (CE). The current to the RE must be small, because a large current would result in errors in measurement. When an electrochemical reaction takes place, a current is detected whose source is the correction of the actual voltage to the required one. A widely used method is cyclic voltammetry (CV). A triangular voltage is imposed and the resulting current is monitored. By plotting current density versus voltage a cyclic voltammogram is obtained. From this the decomposition voltage can be determined.

2.3 Nanobubbles

Gas bubbles in liquids are easily produced with a tube immersed in a liquid on one side. When a pressure is applied on the other side, a gas bubble will form. This method is a possibility to measure the surface tension γ of the liquid.[31] The difference in pressure $\Delta p_{\text{Laplace}}$ between a bubble and the surrounding system predicted by the Laplace-Equation:[32]

$$\Delta p_{\text{Laplace}} = \frac{2\gamma}{r} \tag{8}$$

The pressure within a bubble is reciprocal to the bubble's radius r. For a bubble at a surface r is the radius of curvature. This means the smaller the bubble, the higher the internal pressure. Therefore small bubbles should dissolve according to Henry's Law. It states that the rate of dissolution of a gas is increased when its partial pressure is high. As the bubble size decreases, the internal pressure increases, and the rate of dissolution of the gas increases even more. The process is self-accelerating. Following this theory, small bubbles should be unstable.

First evidence for the existence of stable bubbles with nanometer size was reported by Parker et al.[1] They discovered long range hydrophobic interactions with surface force

measurements. There were discontinuities in the force-distance curves which they attributed to the existence of submicroscopic bubbles at the interface. These small bubbles led to bridging in between the surfaces, hence increased the attractive forces. The bubbles forced the surfaces into contact.

The first pictures of nanobubbles were recorded with an Atomic Force Microscope (AFM) on hydrophobic surfaces by two independent groups in 2000.[2, 33] Ishida et al. measured force-distance curves as well. They showed enhanced attractions when bubbles were present.[33] This confirmed the results of Parker et al. Most studies on surface attached nanobubbles were done with AFM.[5, 34, 35] Usually, AFM is operated in tapping mode, where the cantilever oscillates close to its resonance frequency and interacts with the scanned sample.[36, 37] Other techniques were also employed, like spectroscopic methods[38] and the QCM[39-43] (see chapter 2.3.1).

The most common approach to produce surface-attached nanobubbles is the solvent-exchange method.[2] The substrate is immersed in ethanol or other alcohols. The ethanol is replaced with water and nanobubbles are formed on the substrate. During the replacement a thin film of ethanol stays at the samples surface. This results from the hydrophobic nature of the substrate. The alcohol eventually dissolves in water, but the air that was dissolved in ethanol does not.[34, 44] Air is more soluble in alcohols than in water thus air stays at the interface forming bubbles. This technique relies on supersaturation and it can be performed with various gases dissolved in ethanol.[38, 45] The gas can be replaced by organic liquids that lead to formation of small droplets.[46]

Another possibility to produce nanobubbles at surfaces is electrochemical gas evolution.[47, 48] The bubbles evolve due to electrochemical decomposition of water. The gas is either hydrogen or oxygen, depending on the electrode.

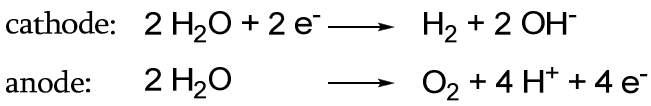

Many factors influence the formation and properties of nanobubbles.[5, 34] Those are the used solvents,[49, 50] substrates and their preparation,[3, 44] gas type,[45] and temperature.[51] The stability of nanobubbles is a phenomenon not yet explained.[52, 53] The observed

contact angles of nanobubbles exceed the contact angles (measured through the denser medium) of macroscopic bubbles.[3] Therefore nanobubbles are shallow lenses with a big radius of curvature. Those shallow bubbles exhibit a smaller Laplace pressure than hemispherical bubbles with identical volume, according to equation 8. This does not change the internal pressure to values that inhibit self-enhancing dissolution.[5] High contact angles cannot fully explain the stability of surface nanobubbles.

2.3.1 Nanobubbles on QCM

The major part of the studies on surface-attached nanobubbles was done with AFM. The obtained pictures of the nanobubbles are the benefit of this technique. Unfortunately, the AFM is susceptible to artifacts and incorrect measurement. Therefore other surface sensitive techniques to measure nanobubbles should be employed, as well. This is necessary to gain further information about the properties of nanobubbles.

Bubbles and nanobubbles have been studied on the QCM. Carr et al. electrochemically generated hydrogen from an aqueous acidic solution.[54] They performed CV to produce the gas. Simultaneously, they measured the frequency shift of a gold-coated quartz crystal. In their discussion, only positive frequency shifts were considered, since they assumed bubbles to decrease the coupled mass on the QCM. They neglected the fact that in their figure 1B a negative frequency shift of about 3 Hz can be found. This negative frequency shift occured between –0.4 V and –0.5 V (with respect to SCE) which corresponds to the first evolution of H_2. In a subsequent paper of the same group they changed the WE material to platinum.[28] The scanned potentials were both negative and positive, thereby producing Cl_2 at positive potentials and H_2 at negative ones. Caused by the broad range of the potential, a lot of different reactions took place. This led to an interference of the frequency shifts which were caused by the different reactions at the electrode. Frequency shifts could not be assigned to single processes. In both papers the descussion covered macroscopic bubbles only.

Another set of experiments was performed by the Craig group.[42, 55] This work mainly aimed at improved surface cleaning by inducing nanobubbles at the surface. The nanobubbles were produced by electrochemical means. A voltage was applied to develop

hydrogen on the quartz crystal. This should remove adsorbed proteins, hence it resulted in positive frequency shifts relative to the coated crystal. Replacement of the protein by nanobubbles was found and removal of the bubbles was possible with phosphate buffer. Positive Δf were found as a result of the removal of proteins.

Formation of nanobubbles on a QCM without electrolysis of aqueous solutions were either done by solvent-exchange procedure[40] or by water saturated with gas.[43, 56] Zhang[40] and Yang et al.[56] reported an increase of resonance frequency when surface nanobubbles were present. The existence of surface nanobubbles was confirmed by AFM measurements. Those bubbles exhibited large contact angles and they decreased the coupled mass to the crystal. Enhanced adsorption of polystyrene nanoparticles due to long-range hydrophobic interactions was studied by Seo et al. This is the only known publication to report negative frequency shifts in conjunction with nanobubbles. Increased coupled mass on the quartz crystal did not arise from gas at the solid-liquid interface. The polystyrene particles caused the negative Δf. Polystyrene adsorbed onto the QCM. This was facilitated by the bridging of the gaseous phase between the particles and the quartz crystal.

All of the publications mentioned here reported on positive frequency shifts as a result of surface-attached bubbles. This is in accordance with classical theories (see chapter 2.1). The nanobubbles were stable and did not dissolve. This stability was supported by the high contact angles of the gas-liquid interface.

2.4 Slip

In fluid dynamics different boundary conditions exist for the velocity of a liquid at a solid-liquid interface. When a Newtonian liquid flows through a tube, the highest velocity of the liquid is found in the middle of the tube. A problem of description arises when approaching the solid-liquid interface. Most of the time, it is assumed that at the solid-liquid interface the liquid exhibits the same velocity as the wall, which is zero for most systems. This assumption is called “no-slip” boundary condition (Figure 4 a).[57, 58] The first description of this was provided by Bernoulli in 1738. The velocity of the liquid can also be nonzero at the wall. This is called slip (see Figure 4). In complex fluids, like

polymer melts, slip is known and studied.[59, 60] In Newtonian liquids it was long assumed that slip is inexistent.

To characterize slip it is convenient to use the slip length b_s. The slip length is the distance from the interface to the plane of zero shear (see Figure 4). Slip occurs when molecules at the interface interact less with the solid wall than with their neighboring molecules. Slip can occur in different magnitudes. The slip length can be either finite (Figure 4 b) or infinite (Figure 4 c). The latter case leads to plug flow.

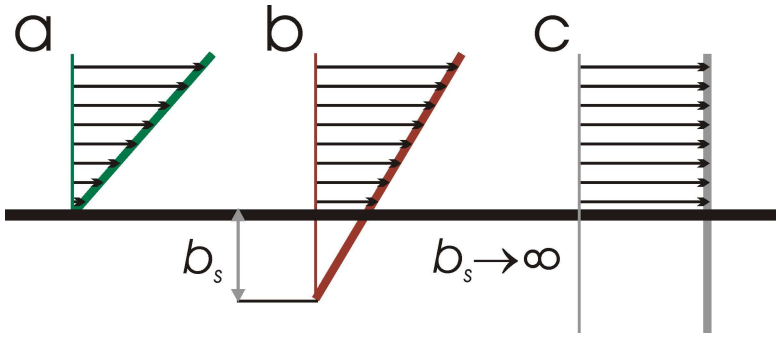

Figure 4: Profile of velocity for a fluid next to a solid-liquid interface. **a**: no-slip boundary condition, velocity is zero at the wall. **b**: b_s is finite, nonzero velocity of the liquid at the interface. Velocity profile is extrapolated to plane of zero shear, distance from plane of zero shear to interface is slip length b_s. **c**: perfect slip, velocity of the liquid is identical at every place. The slip length tends to infinity.

In the mid-20th century the no-slip boundary condition was established for Newtonian liquids.[58] No experimental evidence existed that showed slip at the interface. This was caused by the size of b_s in Newtonian liquids, which is in the order of nanometers. To investigate slip there is need of a method with a spatial resolution in the regime of the slip length. Techniques employed to investigate flow close to the solid-liquid interface are tracer experiments,[61, 62] especially fluorescence recovery after photobleaching (FRAP),[63] surface forces apparatus,[64] AFM,[65] capillary techniques,[66, 67] and QCM.[68-70] Slip in Newtonian liquids was found in these studies.

Assumed effects that lead to slip are the wetting behavior of the liquid, surface roughness, shear rate, nanobubbles respectively gas films, and other parameters.[58] There is still controversial discussion about their degree of influence on slip. The wetting of the surface by the liquid is quantified by the contact angle. If contact angles are high, the interactions between liquid and solid are small. With weak interactions the liquid should

slide more easily at the interface.[64, 69] How surface roughness and shear rate influence interfacial slip is not clear yet. For a system with surface nanobubbles slip is inhomogeneous. When assuming $b_s = 0$ for solid-liquid interfaces (applying a "no-slip" boundary condition) and $b_s \rightarrow \infty$ for liquid-gas interface, there is an effective slip length of $0 < b_s < \infty$ for nanobubbles.[71] For nanobubbles produced by solvent-exchange method this should be valid. They exhibit high contact angles (see chapter 2.3), thus the liquid can easily slide over the bubbles. This is not true for every system with surface attached nanobubbles. When the surface is highly structured, like ultra hydrophobic surfaces, stable nanobubbles may have other geometries than shallow lenses. Small gaseous domains occur, because the liquid cannot penetrate into the grooves or pits of the substrate. If the three-phase contact line is pinned, the bubbles can exhibit small contact angles. Their stability does not depend on their contact angle to the same extent as for nanobubbles on unstructured surfaces. Bubbles with a pinned three-phase contact line were found to reduce slip. They act like surface roughnesses and trap the liquid in between them. This leads to negative slip lengths. [72, 73]

A slipping layer can be interpreted as a layer of reduced viscosity. The slip length can be expressed with:[39, 58]

$$b_s = \left(\frac{\eta_L}{\eta_f} - 1 \right) \cdot d_f \tag{9}$$

d_f is the thickness of the layer with reduced viscosity. An acoustic slip length $b_{s,\,ac}$ can be defined as:

$$b_{s,\,ac} = \left(\frac{\rho_f}{\rho_L} - \frac{\eta_L}{\eta_f} \right) \cdot d_f \tag{10}$$

This provides the possibility to express the slip length by terms of Δf of a quartz crystal. On the QCM reduced viscosities introduce positive frequency shifts according to equation 5. Equation 5 can be expressed as:

$$\Delta f = -m_f \cdot \frac{2n \cdot f_F^2}{Z_q} \left(\frac{\rho_f}{\rho_L} - \frac{\eta_L}{\eta_f} \right) \tag{11}$$

Applying equation 10 to 11, an equation that is similar to the Sauerbrey equation (1) can be found

$$\Delta f = \rho_f \cdot \frac{2n \cdot f_F^2}{Z_q} b_{s,ac} \tag{12}$$

The slip length can be calculated like the Sauerbrey thickness (compare to eq. 2). The latter is equal to negative $b_{s,ac}$. With the QCM it is possible to measure and quantify the slip length in Newtonian liquids.

2.5 Hofmeister Series

In the 1880s and 1890s Franz Hofmeister did a series of experiments on the effects of salts on proteins.[74] He carried out several experiments on the clouding of protein solutions after the addition of salts. An influence on the precipitation of proteins was found depending on salt-type. This influence is called Hofmeister effect or specific ion effect. The investigated ions were arranged in two series where one is for anions and the other for cations. Hofmeister himself proposed the order for salts and not for independent anions and cations. The Hofmeister series[75] is mostly written as shown in Figure 5. Therein are the anion and cation series. Ions with salting-out effect, thereby destabilizing proteins, are called kosmotropic and those with stabilizing properties are called chaotropic. In general the specific ion effects are more pronounced for anions.

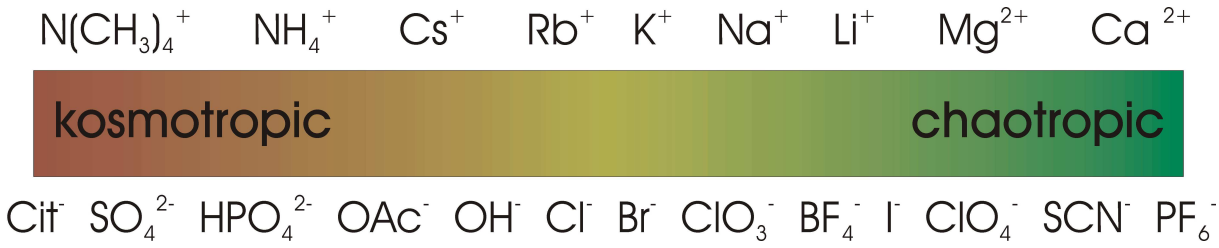

Figure 5: Hofmeister series.

Up to date it is still not clear why ions according to this order affect proteins, polymers, pH measurements, and ion binding to interfaces.[76] The latter includes the influence of ions on surface tension.[77] One of the main problems is that the Hofmeister series is not universal. There are several Hofmeister series with slight differences, depending on the examined system. For instance partial or total reversal of the series

could be found. This is either induced by concentration changes[78] or by surface charge.[79] This shows the complexity of the parameters impacting the specific ion effects. The factors governing the interactions of the ions are their charge density, counterions, headgroups of proteins and surfactants, concentration of the salt, pH value, polarizability (soft and hard ions), hydration, and others.[75, 76, 80] Even the fundamental cause for the Hofmeister series, if it is a bulk effect or a surface specific effect, is not solved. One of the main factor seems to be the polarizability of ions which must not be considered without the polarizability of counterions and interacting species (protein headgroups, polymers, inorganic particle, etc.). The concept of "like likes like" or "like seeks like" was introduced by Collins.[75] This assumption explains the findings in many studied systems but not in all. Other influences, as mentioned above, must be considered.

Changes in surface tension of water due to added salts are also attributed to ion specific effects that are correlated to the Hofmeister series.[81] Ions are repelled from an air-water interface, because it is more favorable for them to be hydrated then to be at the surface. Hence salts increase surface tension, their concentration in the bulk is higher than at the surface. This is not valid for acids, H_3O^+ molecules accumulate at the interface like surfactants.[75, 81] The increase in surface tension should have positive influence on nanobubble stability and stiffness.

Attempts to quantify the Hofmeister series were done, but the assumed coefficients cannot predict the ion specific effects.[80] Those do not take into account the complexity of non-dilute systems that follow this series.

3 Experimental

3.1 Materials

All water used for experiments was of ultra-pure grade (18.2 MΩcm, arium®611VF, Sartorius, Germany). Salts and surfactants of this study are listed in the appendix (chapter 8). Quartz crystals (Fil-Tech, MA) were of AT-cut type with a resonance frequency of 5 MHz and a diameter of 1 inch. The electrodes of the crystal were either of gold or of silver (thickness: 200 nm). As an adhesive layer of chromium (10 nm thick) was introduced. The mount for the crystals was purchased from Maxtec, CA.

3.2 Setup

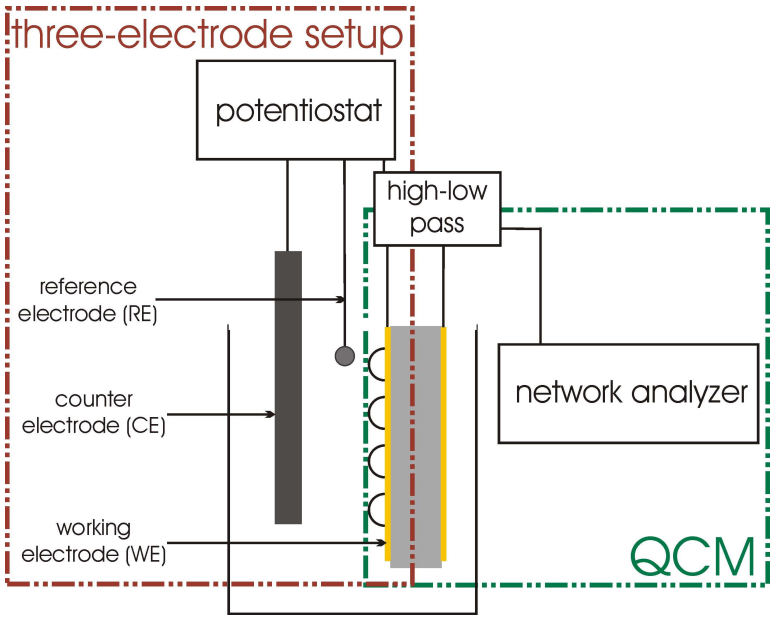

Figure 6: Schematic setup for EQCM.

For EQCM measurements a three-electrode setup was employed. The front electrode of the crystal was used as WE and a platinum sheet as CE. All potentials were determined versus a saturated calomel electrode (SCE, KE11, Sensortechnik Meinsberg, Germany) which was the RE. To adjust potentials the electrodes were connected to a potentiostat (PGU 10V-1A IMP, Jaissle, Germany) whose potentials were given by a function generator (Agilent 33220A, Agilent Technologies, CA). The high frequency signal to drive the quartz crystal was controlled by a network analyzer (HP4396A, Hewlett Packard, CA). To separate the high frequency signal of the network analyzer from low

frequency signals, the voltages of the potentiostat, a self-built high-low pass was introduced. A schematic setup is given in Figure 6. Data analysis of the QCM signals was done by impedance analysis and the software QTZ.

3.3 Procedure

Preparation of the quartz crystal before the measurements was done by cleaning the crystal with a UV/ozone cleaner (Bioforce Nanosciences, USA) for 20 min. Cleaning of the crystals in between a set of measurements was done with Piranha solution (H_2O_2 : H_2SO_4; 1 : 3).

For the production of bubbles square wave voltages were applied on the WE. Starting from –0.5 to –2 V vs. SCE the voltage was decreased in 0.1 V steps, each step was applied for two minutes. Between those steps 0 V vs. SCE was applied for two minutes. During the whole time frequency and bandwidth shifts were recorded with the program QTZ. Up to four harmonics (n = 1 to 7) were measured at the same time. The drive level of the quartz crystal was 15 dBm.

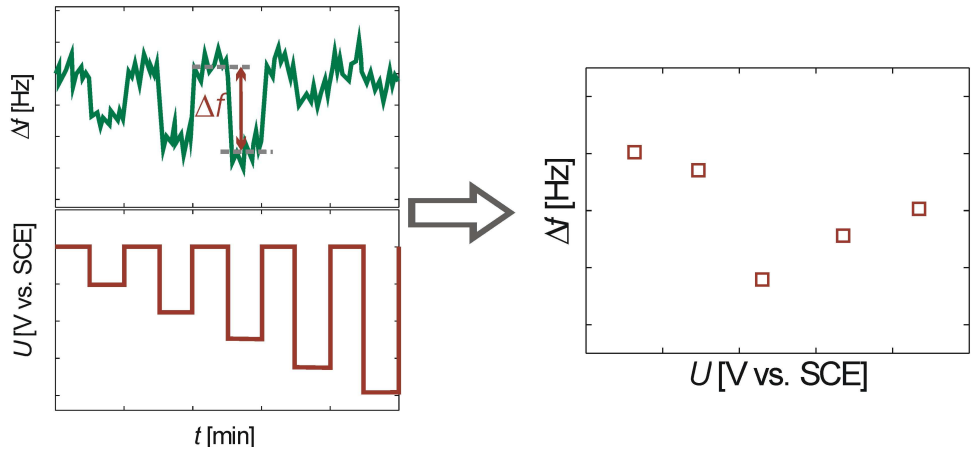

Figure 7: Determination of frequency shift for analysis. Time-averaged values of the frequency shift were calculated relative to the baseline and plotted versus the potential.

For analysis and easier interpretation of the data, the frequency and bandwidth shifts were averaged over time of each applied voltage. Since a shift of the baseline (potential 0 V vs. SCE) cannot be eliminated, the averaged frequency and bandwidth shift before and after the negative voltage is subtracted from the determined values of Δf and $\Delta\Gamma$ (see

Figure 7). Therefore only the *step* is considered that is induced by changes at the electrode, when a voltage is applied. All added lines in those diagrams are to guide the eye, the values in the range between two points are not known.

4 Results and Discussion

4.1 Preliminary Experiments

In the first studies the focus was on the resulting frequency and bandwidth shifts induced by the formation of bubbles at the electrode surface. Therefore the control of the electrolyte was of minor concern.

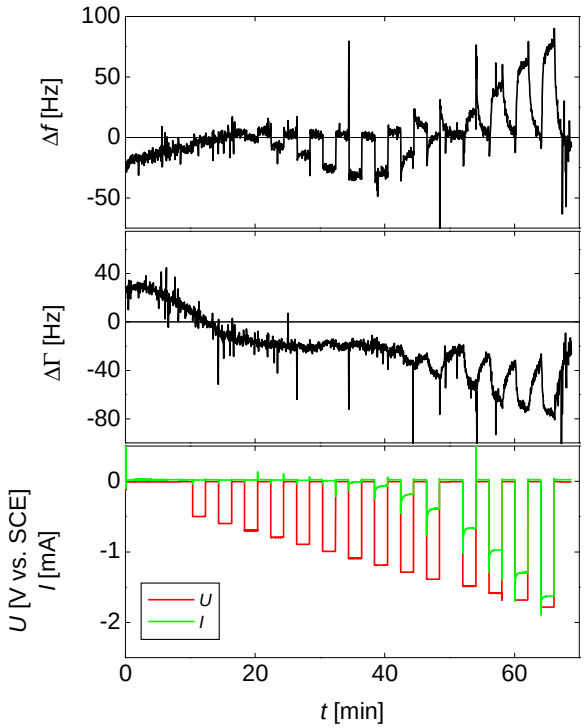

Figure 8: Measurement of 1 mol/L KNO_3 solution. Δf and $\Delta\Gamma$ were determined for the 15 MHz overtone (n = 3).

As an example the measurement with a 1 mol/L KNO_3 solution is shown in Figure 8. The signals of the QCM are easily interpreted, because no significant baseline shifts occured. In this measurement two different behaviors of Δf and $\Delta\Gamma$ were obtained. For small negative potentials the observed shifts in frequency were negative while the bandwidth showed nearly no response. Frequency shifts occur when the negative voltage is applied. No kinetics of formation is observed. When the negative potential is switched off Δf reassumes zero. The shift at the beginning and the one at the end of the negative potential are very abrupt.

After decreasing the voltage between the WE and the RE further, Δf exhibits positive values. The bandwidth alters its behavior as well and it decreases. Some kinetics can be observed. When a negative voltage is applied, the frequency shift increases quickly. The increase becomes less during the pulse. When the system is disengaged the decrease happens in the same manner.

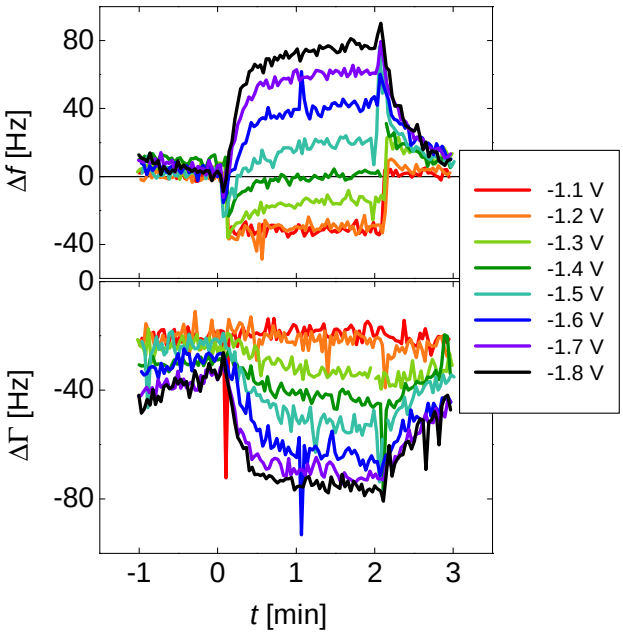

Figure 9: Change of kinetics due to increased potentials at the WE. The time scale was changed to set the start of the applied potential to $t = 0$. After 2 min the potential is switched off. For small negative potentials the shifts in Δf are abrupt. By further decreasing the potential, kinetics of the formation of bubbles can be observed. The time constant of Δf for the initial increase is in the regime of 30 s for all potentials lower than –1.2 V vs. SCE.

The difference between the kinetics of the different voltages can be seen in Figure 9. At $t = 0$ the negative potential is applied to the WE. The change from a rapid decrease of Δf to a slower increase caused by the negative potential can be observed. This initial increase of the frequency shift is steeper the more negative the potential becomes. After approximately 30 s the curve approaches a plateau. The frequency shift is almost constant for the rest of the pulse. The dissolution of the bubbles after the potential is switched off ($t > 2$ min) is slightly slower than for the formation of the bubbles. The initial values of Δf are reached after 1 min. At the beginning of the pulse the formation of hydrogen competes with the dissolution of hydrogen. Those two processes determine the obtained

frequency shifts. For t > 2 min Δf is only governed by the dissolution of H_2. Since the increase of Δf is faster the evolution of hydrogen must be faster than the dissolution for the high negative potentials.

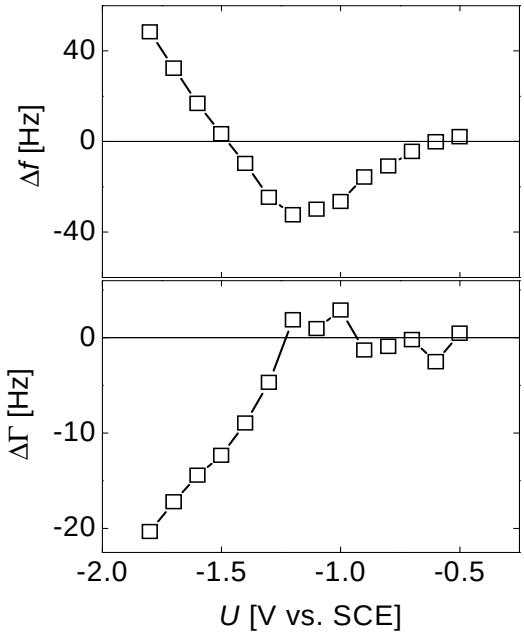

Figure 10: Analysis of the measurement shown in Figure 8. Time-averaged values for shifts in frequency and bandwidth for solution of 1 mol/L KNO_3. Overtone order n = 3 (15 MHz).

The negative and positive shifts can also be found in the plot of the time-averaged frequency and bandwidth shift (Figure 10). This kind of plots is mostly shown in this thesis, since baseline shifts are eliminated. For high negative potentials the explanation of the response of the crystals is straight-forward. Evolution of hydrogen takes place at the WE. Gas decreases the mass coupled to the quartz crystal, relative to the liquid. An increase in frequency shift is expected and experimentally observed. The gas also leads to less damping of the oscillation of the QCM which is reflected in the decreased bandwidth. While the potential is applied, more and more bubbles are formed at the electrode. The frequency shift still increases and the bandwidth shift correspondingly decreases. Bubbles become larger until they detach from the electrode. In the meantime other bubbles are formed and start to grow. After some time equilibrium is reached and the resonance frequency as well as the bandwidth, are constant. In the present case equilibrium is not reached after the two minutes of the negative voltage. After the voltage is switched off,

dissolution of the bubbles takes some time. Their internal pressure is in a moderate regime.

For smaller negative potentials H_2 is also produced at the front electrode of the crystal. The response in frequency indicates an increased coupled mass to the oscillation of the QCM. On the other hand a shift in bandwidth is not visible. Therefore the viscous properties are not changed compared to no applied voltage. These results are not in accordance with classical theories.

The amount of the formed hydrogen can be calculated with Faraday's first law of electrolysis. By assuming the volume of an ideal gas the volume of H_2 released from the electrode can be calculated. At –1.2 V 18 µL of hydrogen gas are formed, this is the voltage resulting in the biggest negative frequency shifts. When Δf changes its sign at –1.5 V, the volume of H_2 is 159 µL. The amount of hydrogen is increased by a factor of 10.

At small negative potentials electrolysis of water is slower than at high potentials. This leads to smaller amounts of H_2 at the electrode. Macroscopic bubbles cannot be formed caused by a kinetic control of the H_2 formation. The gas must build small domains. Since Δf and $\Delta\Gamma$ are constant during the whole pulse their dissolution must be of approximately the same rate as the formation of hydrogen. For small potentials the bubbles are in a dynamic evolution-dissolution equilibrium. Their dissolution is fast due to their high Laplace pressure. The observed nanobubbles are *not stable*. They disappear as soon as the potential is switched off. The bubbles produced by electrochemical means are not like the ones obtained via solvent exchange method. They do not have to exhibit the same properties like high contact angles. High contact angles enhance the stability of nanobubbles. For this reason it is likely that bubbles produced by electrochemical means exhibit smaller contact angles.

Bubbles of nanoscopic size obtained via electrochemistry have other properties than macroscopic ones. This is in agreement to experiments with nanobubbles produced by other techniques. As stated in chapter 2.3 the Laplace pressure of small bubbles is very high. When a surface-attached bubble is exposed to a tangential shear field the bubble is deformed. This deformation induces a local change in Laplace pressure $\Delta(\Delta p_{\text{Laplace}})$. The

radius of curvature *r* becomes smaller on one side of the bubble, and larger on the other. A normal force onto the surface of the bubble is the result (see Figure 11). These normal forces oppose the deformation of the bubble.

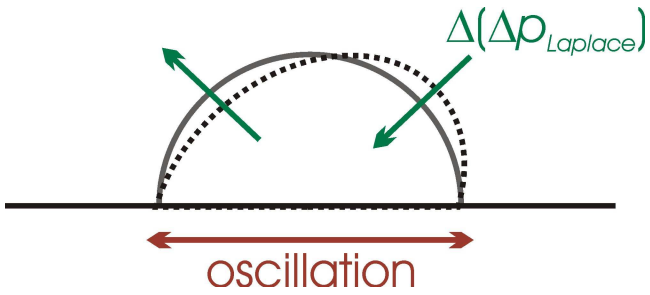

Figure 11: Change in Laplace pressure caused by a tangential oscillation. The grey line depicts the undeformed bubble and the black dashed line the deformed bubble. On the left hand side the radius of curvature is increased hence the Laplace pressure is decresed. On the right hand side the Laplace pressure increases due to the reduced radius of curvature.

To figure out how the change in Laplace pressure governs the properties of bubbles, an analytical estimation can be made. For a shear field the change of the internal pressure depends on the shear angle θ of the bubble:

$$\Delta\left(\Delta p_{\text{Laplace}}\right) \propto \frac{\gamma}{r} \cdot \theta \tag{13}$$

Here *r* is the radius of curvature in the undeformed state and γ the surface tension. The change in Laplace pressure counteracts the shear-induced deformation of the bubble. The viscous shear stress σ_{vis} must be compared to the change in internal pressure to get information on the deformation of the bubble. The viscous shear stress is given as:[39]

$$\sigma_{\text{vis}} = \omega\eta \cdot \frac{u_0}{\delta} \tag{14}$$

where η is the viscosity of the liquid, $\omega = 2\pi f$ is the angular frequency, u_0 is the amplitude of the oscillation, and δ is the decay length of the shear wave. The ratio of surface tension and radius is equal to the bubble's stiffness and ωη is the stiffness of the surrounding liquid. When $\frac{\gamma}{r} << \omega\eta$, the bubble is relatively soft and deforms under tangential shear. In this case the expected positive frequency shifts are obtained. The mass coupled to the crystal is decreased due to the gaseous phase. If $\frac{\gamma}{r} >> \omega\eta$, the bubble

is relatively stiff and stays undeformed. In this case the adjacent liquid is dragged along with the movement of the quartz crystal. The bubbles act like surface roughnesses and trap the liquid in between them. This trapped liquid increases the mass on the QCM, consequently this leads to a decrease in frequency. This is in agreement with the results of simulations for stationary flow, when the gas-liquid-solid contact line is pinned.[72, 73] They also behaved stiff and trapped the liquid between the bubbles. Negative slip lengths were found for the bubbles with a pinned three-phase contact line.

Assuming water as liquid ($\gamma = 72$ mN/m, $\eta = 1$ mPas) and a quartz crystal with 5 MHz as resonance frequency, the critical radius r_{crit} between soft and hard bubbles is about 2 μm. This can be calculated with:

$$r_{crit} \approx \frac{\gamma}{\omega\eta} \tag{15}$$

When the bubble is of nanoscopic size (< 2 μm), it is stiff and induces negative Δf. Bubbles with a larger radius than 2 μm act like a heterogeneous interface. The large bubbles lead to positive Δf. These results were supported by FEM simulations done by D. Johannsmann (see chapter 6). The increase of the hydrodynamic drag can only happen if the formed bubbles exhibit contact angles around 90°. When the bubble is shallow, like the ones obtained by solvent-exchange method, the liquid can stream above the bubble without any hindrance. The other extreme, a truncated sphere, can rotate about the point of contact angle therefore would not enhance the hydrodynamic drag.

The slip length at the interface can be calculated with equation 12 from Δf shown in Figure 10. The values used were $f_F = 5$ MHz, $n = 3$, and $\rho_f = 1$ kg/L. By assuming the density of water as the density of the slipping layer $b_{s,\,ac}$ is underestimated. Since the real density is unknown this approximation must be made.

Figure 12 shows the calculated values for the slip length. The shape of the curve corresponds to the data of Δf shown in Figure 10. Δf and $b_{s,\,ac}$ are proportional. At small negative potentials $b_{s,\,ac}$ is negative. This implies that a layer with the thickness of $b_{s,\,ac}$ sticks to the substrate and moves with its velocity. On the quartz crystal the movement is the oscillation with its resonance frequency. The values received show that the viscous

sample sticks to the crystals surface up to 2 nm. As already mentioned this value is just an approximation. The real slip length b_s should be bigger than the obtained values of $b_{s,\,ac}$. The real density of the observed layer must be smaller than 1 kg/L because it consists of electrolyte and gas.

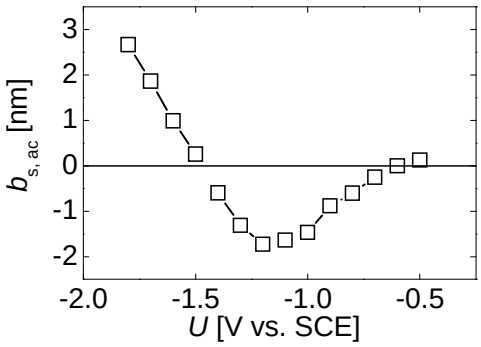

Figure 12: Slip length $b_{s,\,ac}$ for the measurement with 1 mol/L KNO_3. The values shown in Figure 10 were used to calculate $b_{s,\,ac}$ with equation 12.

For large negative potentials the sign of $b_{s,ac}$ changes. Slip is induced through the bubbles at the interface. The slip length is in the nanometer regime that is expected for Newtonian liquids.

Even though the values calculated for $b_{s,\,ac}$ are smaller than the real ones it is possible to measure slip lengths with the QCM in the nanometer regime. The obtained sizes were expected for slip in a Newtonian liquid. Since the slip length is proportional to the frequency shift it is not necessary to calculate $b_{s,\,ac}$. When Δf is negative, $b_{s,\,ac}$ is negative as well and vice versa.

To have a closer look at the characteristics of this trapped water the overtone dependence is considered. This should yield more information about the properties of the sample in the vicinity of the WE. For this purpose $\Delta f/n$ and $\Delta\Gamma/n$ are plotted versus the overtone order n. This refers to a Sauerbrey behavior. The same is done for $\Delta f/n^{0.5}$ and $\Delta\Gamma/n^{0.5}$ to check for scaling according to Kanazawa (see chapter 2.1). In the following these plots are called Sauerbrey and Kanazawa plot, respectively. The data are exemplarily shown in Figure 13 for the 1 mol/L KNO_3 solution.

The obtained plots should show horizontal lines for the frequency and bandwidth shifts when the system follows the assumed overtone dependence. It is found that the sample at the electrode behaves more like a stiff film (Sauerbrey, left side Figure 13) than a viscous liquid (Kanazawa, right side Figure 13). The fact that frequency shifts are proportional to the overtone order was found for most measurements. This result supports the results discussed beforehand. Although only water and gaseous domains were present, the layer is not viscous. This heterogeneous interface does not lead to Kanazawa scaling. The water in between the bubbles is trapped so tightly that it moves with the quartz crystal as if it adheres to the surface. The overtone dependence supports the theory of the trapped liquid at the electrode of the QCM.

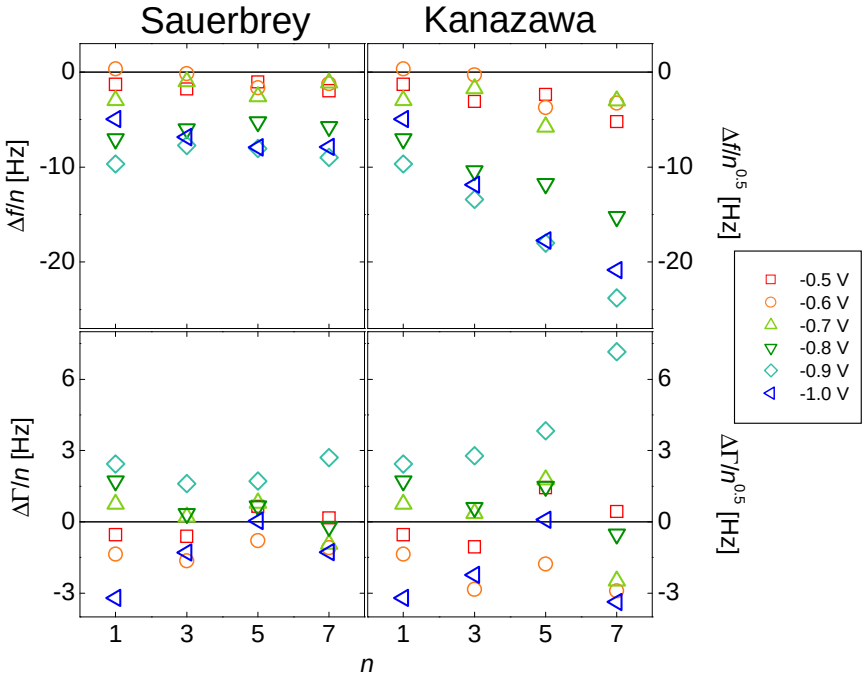

Figure 13: Sauerbrey plot (left) and Kanazawa plot (right) determined from time-averaged values of Δf and $\Delta\Gamma$. Plots are given for small negative potentials (–0.5 V to –1.0 V). When the values are parallel to the abscissa the shifts are according to the respective theory. The frequency shift behaves like Sauerbrey, Δf is proportional to n.

Shifts in bandwidth are harder to interpret, mainly caused by their smaller size. There is also a support for Sauerbrey type behavior, because a perfect Sauerbrey film does not show a shift in bandwidth. A viscous sample entails a bandwidth shift equal to the negative frequency shift. The small shifts of bandwidth indicate that there is some internal friction, but dissipation is not significant as expected for a viscous medium.

As a summary, in these first experiments it was found that small bubbles do not lead to positive frequency shifts. This is not in accordance to the classical theory where positive frequency shifts are expected on bubble formation. The results can be explained by a more elaborated theory that includes the increased internal pressure and its change due to bubble deformation. The nanobubbles are so stiff that they trap the water, which is dragged along with the movement of the crystal. Nanobubbles can *reduce* slip in MHz shear fields. This was found accordingly for stationary flow. The slip length was negative for bubbles of nanoscopic size. The trapped liquid behaves like a stiff film and not like a viscous liquid, which can be concluded from the overtone dependence of Δf. No Kanazawa scaling, but rather Sauerbrey scaling is found in the experiments.

4.2 Reproducibility

To check the reproducibility of the shifts in frequency and bandwidth, different measurements with the same electrolyte were evaluated. Aqueous solutions of 0.25 mol/L $NaNO_3$ were measured most often. The statistics of the measurements is examined to

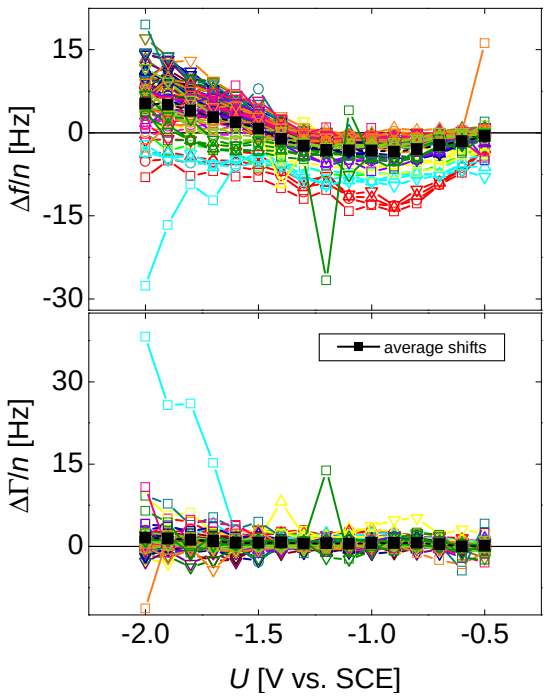

Figure 14: Measurements of aqueous solutions with 0.25 mol/L $NaNO_3$. Identical color implies same measurement on different overtones. Black squares denote averaged data over all acquired values.

quantify the reproducibility of the observed QCM response. For a better overview of the data all values are divided by the overtone order *n*. This is possible, because the load follows Sauerbrey scaling (see chapter 4.1). The time-averaged data of all 19 measurements with 0.25 mol/L sodium nitrate solutions are plotted in Figure 14. The single measurements are not labeled, the black squares represent data averaged over all measurements.

The frequency shifts vary over a broad range and it can clearly be seen that the reproducibility is a problem. Similar voltage dependence is found throughout the various measurements. Starting with Δf of approximately zero, the data shows a minimum around –1.0 V vs. SCE. At more negative voltages the frequency shifts increase again. For $\Delta\Gamma$ values around zero are observed. The bandwidth stays almost constant during all measurements. Preparation of the sample and the electrolyte was not considered, it will be discussed in the next paragraph. In the following only frequency shifts will be discussed, because bandwidth shifts do not show any significant changes.

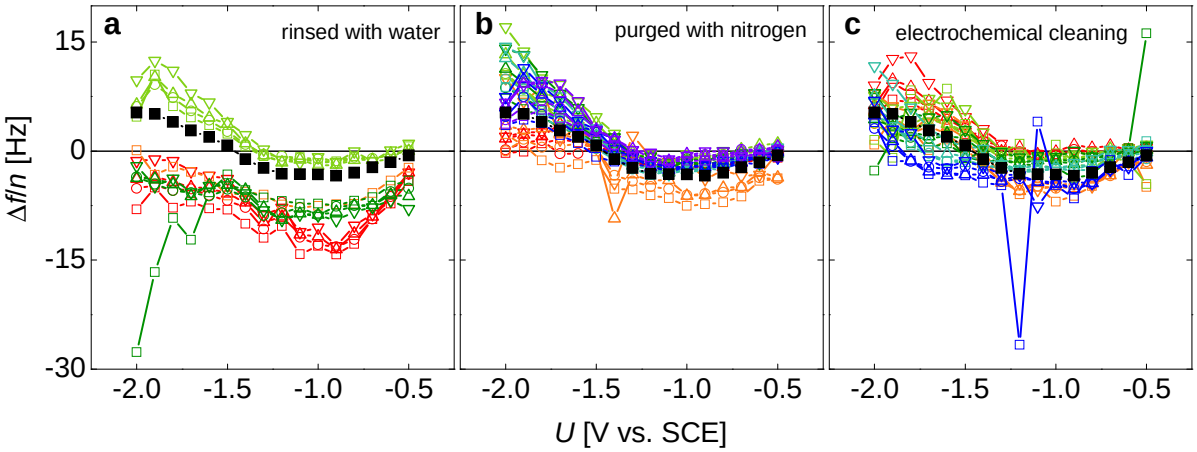

Figure 15: Frequency shifts for 0.25 mol/L $NaNO_3$, with variation of intermediate cleaning. **a**: crystal was cleaned with ultra pure water only. **b**: with additional purging of the electrolyte with nitrogen for 20 min. **c**: in addition to the before mentioned cleaning method an electrochemical cleaning with a 0.1 mol/L H_2SO_4 solution was conduced. Black squares are the averaged $\Delta f/n$ calculated from all measurements.

The measurements shown above were not arranged according to the preparation of the electrolyte or the quartz crystal. The crystal was used for several measurements, intermediate cleaning was changed. In Figure 15 different preparation methods are

compared. In the left graph the crystal was rinsed with ultra pure water between measurements (Figure 15 a). The frequency shifts exhibit a broad variation. Obviously cleaning by this method is insufficient to produce reliable results. By letting a stream of nitrogen flow through the electrolyte in order to remove absorbed gas, a better reproducibility should be attained. By washing the electrolyte for 20 min with N_2 an improvement of reproducibility could be achieved (Figure 15 b). Similar results were obtained when an additional electrochemical cleaning was carried out (Figure 15 c). For this purpose the crystal was immersed in 0.1 mol/L H_2SO_4 and cyclic voltammetry was performed. Five cycles with a sweep from 0 V to –2 V and a scan rate of 200 mV/s were applied to the system. After this, cleaning with water and the preparation with nitrogen was carried out additionally. A further improvement of the reproducibility relative to purging with nitrogen was not found. From these results it can be concluded that a thorough cleaning is important to obtain good results.

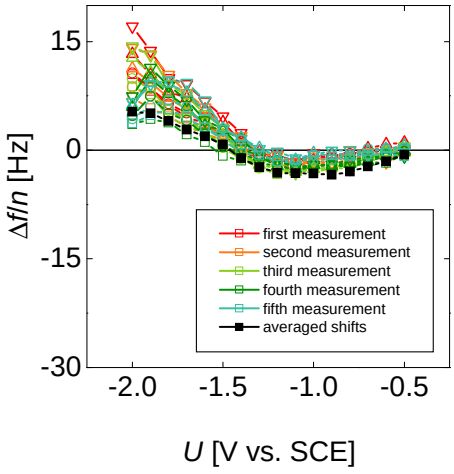

Figure 16: Frequency shifts of five measurements conduced on the identical quartz crystal. The electrolyte was 0.25 mol/L $NaNO_3$. Colors indicate the different measurements, different shapes refer to the overtone order. Those were from n = 1 to 7. Black squares are data averaged over all measurements.

The results for the electrolyte purged with nitrogen might be misleading since five of the shown seven measurements were conducted on the same crystal. These are shown in Figure 16. The axes are scaled identically to Figure 15 to achieve better comparability. It is obvious that the results exhibit less variance. To quantify the reproducibility of the results the standard deviation s was calculated with:

$$s = \sqrt{\frac{1}{N}\sum_{i=1}^{N}\left(x_i - \langle x \rangle\right)^2} \tag{16}$$

and was introduced into Figure 17 as error bars. N is the number of measured values, x_i is the i^{th} data point and $\langle x \rangle$ is the average value.

The average data for the various cleaning procedures and the measurement on one quartz crystal are plotted in Figure 17. Rinsing with water is insufficient to result in reproducible frequency shifts. The variation of the data is, by far, the broadest. It seems that washing the electrolyte with nitrogen is a crucial step. All graphs with this cleaning step (Figure 17 b, c, d) show significantly smaller standard deviations and $\Delta f/n$ is less negative. This result is improved by the usage of the same crystal for five measurements. The electrochemical cleaning decreases the variance, relative to cleaning with water as well (Figure 17 c). If this improvement is caused by the electrochemical cleaning or just by the streaming with nitrogen is not known. Experiments with electrochemical cleaning as the only preparation step were not conducted.

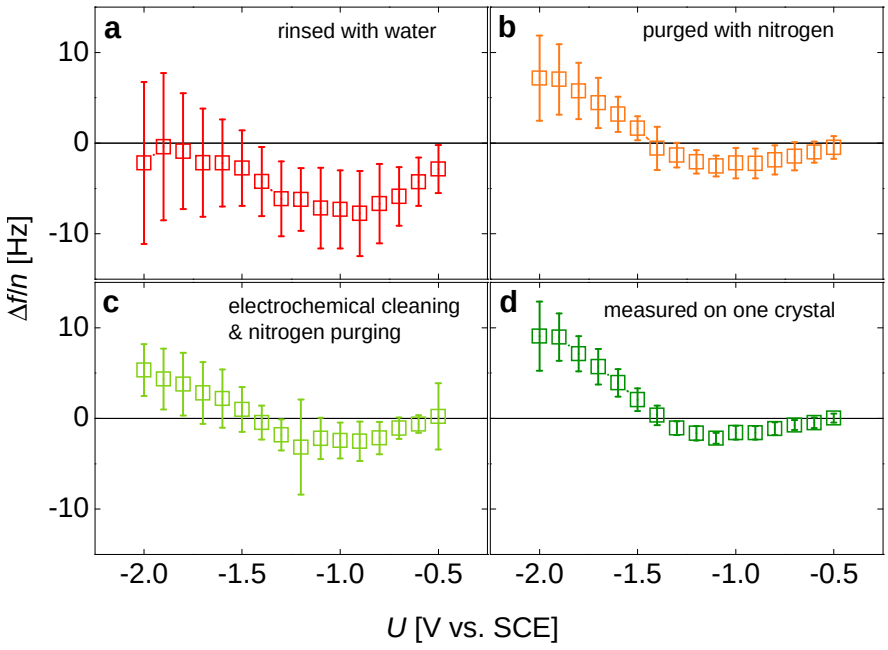

Figure 17: Average values for the various cleaning methods with standard deviation as error bars. **a**: crystal rinsed with water. **b**: additional cleaning of the electrolyte with N_2. **c**: additional electrochemical cleaning in 0.1 mol/L H_2SO_4. **d**: same cleaning as in b though all measurements were done on the same crystal.

To obtain very accurate data it is best to use the same crystal for all measurements which is practically not feasible. The quartz crystal can be contaminated between sets of measurements. This set of data showed the smallest variance. Therefore the crystal, or the electrode surface of the crystal, has an important influence on the measured frequency shifts. The surface topology of the electrode can be changed due to the history of a quartz crystal which might be cleaned several times with Piranha solution. This mixture of H_2O_2 and H_2SO_4 can lead to an etching of the electrode. An enhancement of the electrodes roughness is the result. These roughnesses can act as nucleation sites for bubbles. The eased formation of bubbles should lead to more negative Δf. When the roughnesses are pits the gas phase can be formed in those and lead to less mass coupled to the QCM. Definite statements about the influence of surface roughness cannot be made.

To summarize this chapter, reproducible results can be obtained by precise preparation of the employed electrolyte and the quartz crystal. The streaming with nitrogen to remove solved gas and electrochemical cleaning are crucial steps. The biggest influence is the history of the crystal. Quartz crystals were used for a set of measurements and cleaned in between with Piranha solution, the electrodes are rough. To avoid this influence the same crystal has to be used for all measurements. This is practically not realizable with every measurement. Therefore it is best to use an electrochemical cleaning and purge the electrolyte with nitrogen.

4.3 Addition of Carbon Dioxide

The improvement of reproducibility of the frequency shifts was obtained by purging the electrolyte with N_2, as it was mentioned in chapter 4.2. This improvement should be induced by the removal of gases solved in the liquid. To further test this hypothesis, CO_2 was dissolved in the electrolyte.

Carbon dioxide was streamed through the electrolyte with a small excess pressure for either 10 or 20 min. After the addition of CO_2 electrochemical measurements were conducted either with or without treatment of the electrolyte with nitrogen. All

measurements were done with the identical quartz crystal to obtain best reproducibility. The time-averaged frequency shifts are shown in Figure 18.

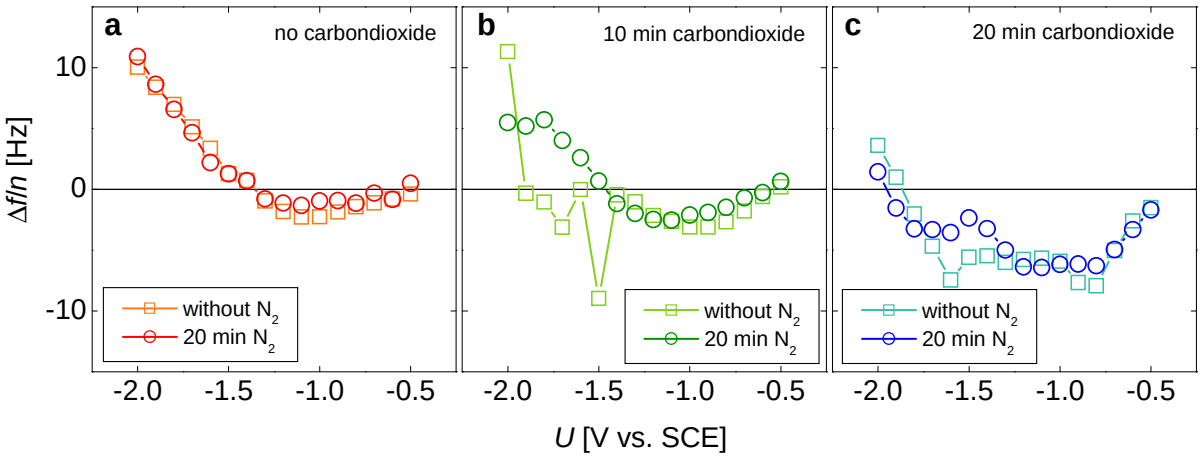

Figure 18: Frequency shift resulting from the addition of carbon dioxide. In an 0.25 mol/L $NaNO_3$ solution different amounts of CO_2 were solved. Measurements were done with and without purging the electrolyte with N_2 (□: no nitrogen; ○: 20 min streaming with nitrogen). All measurements were conducted on the identical quartz. **a**: 0.25 mol/L $NaNO_3$ without treatment with carbon dioxide. **b**: after 10 min of streaming with CO_2. **c**: $\Delta f/n$ after 20 min of CO_2 exposure. Data is averaged over four overtones (5 MHz to 35 MHz).

Frequency shifts are more negative with increasing CO_2 amount in the electrolyte. The mass coupled to the quartz crystal increases. Presumably, this is due to the enhanced formation of small gas bubbles on electrode, resulting in a more effective trapping of the liquid. The enhanced formation of bubbles can be the result of two mechanisms. First it can be induced by the lowered pH value due to the hydrolysis of carbon dioxide to carbonic acid.

$$CO_2 + H_2O \rightleftharpoons H_2CO_3$$

The lowered pH changes the decomposition potential of water at the cathode to values closer to 0 V vs. SCE. Therefore the evolution of hydrogen is enhanced relative to solutions with a pH around 7. The measured pH (WinLab® Data Line pH-Meter with WinLab® Elektrode pH/T30, Windaus Labortechnik, Germany) was 3.90 for the solution streamed 10 min with CO_2 and 3.84 for the one with CO_2 treatment for 20 min. The increased activity of protons a_{H^+} change the decomposition potential φ according to the Nernst equation[30b].

$$\varphi = \varphi_0 + \frac{RT}{zF} \cdot \ln a_{H^+} \quad (17)$$

φ_0 is the standard potential, R the gas constant (8.314 J/K·mol),[82] T is absolute temperature, z is the number of charges per transfer and F is the Faraday constant (96485 C/mol).[82] This change of φ can be a reason for increased coupled mass due to more gas bubbles at the electrode. To quantify this change of the decomposition potential the following values were used. The standard potential φ_0 was –0.2415 V, which is for H_2/H^+ at a platinum electrode vs. SCE at 25 °C.[30c] This standard potential consists of the standard potential for the H_2/H^+ reaction (0 V vs. standard hydrogen electrode (SHE)) and the standard potential of the SCE (+0.2415 V vs. SHE). The number of charges is 1 for protons and the activity of the protons was determined with the pH of the solution. This results in a standard potential of $\varphi_{pH\,7}$ = –0.656 V vs. SCE for neutral electrolytes at 25 °C. For the CO_2 solutions the same calculation leads to $\varphi_{pH\,3.9}$ = –0.472 V vs. SCE with 10 min streaming of CO_2 and $\varphi_{pH\,3.84}$ = –0.469 V vs. SCE for the one with 20 min of streaming. The difference in the potentials of the latter two does not explain the variation in their frequency shifts. It explains the change relative to the pure 0.25 mol/L $NaNO_3$ electrolyte.

The second explanation for the enhanced rate of bubble formation is facilitated condensation of the generated hydrogen. This can be caused by bubbles already formed and consisting of carbon dioxide. The bubbles can be generated by the dissolved CO_2. In those bubbles the hydrogen can dissolve and problems with nucleation of bubbles are bypassed. This must be especially effective for the high concentration of solved CO_2. The differences in frequency shift of the two solutions with CO_2 must base on this mechanism. It is likely that this mechanism leads to the differences in Δf between the pure electrolyte and the electrolyte with CO_2 and not the decrease of the pH.

The streaming with nitrogen does not lead to big differences in the frequency shifts. It is not possible to remove the dissolved carbon dioxide to the point where there is no influence on the formation of bubbles. The improved reproducibility, as stated in chapter 4.2, is based on the removal of substances other than CO_2 or it just depends on the improvement caused by the utilization of the identical quartz crystal.

As a conclusion, dissolved gases strongly influence the formation of nanobubbles by electrochemical means. This can be either by the change of properties of the solution, like in the case of carbon dioxide the pH value, or by the formation of bubbles consisting of dissolved gas. The latter can be induced by changes in temperature, solvent quality or available nucleation sites. These sites can be consequences of the electrochemistry that takes place at the electrode. The pH is lowered by the dissolved CO_2, but this cannot be the only reason, an eased nucleation caused by preformed CO_2 bubbles is more crucial.

4.4 Change of Electrode Material

All experiments discussed to this point were conducted on quartz crystals with gold electrodes. The decomposition of water as well as the formation of nanobubbles can be influenced by the electrode material. One point is the change of the overpotential of hydrogen which depends on the used electrode material. This leads to a change of the measured decomposition voltage of water. For silver the overpotential should be different from the ones for gold but the precise value can change between measurements[83]. The frequency shifts measured on gold electrodes should be found in the same manner on silver, except at other potentials.

Another fact that should be considered is the influence of electrode materials on the kinetics of the hydrogen evolution. Depending on the strength of the metal-hydrogen bond the mechanism at the electrode varies. The reaction rate determining step can change. The reaction mechanism at the electrode can be described either by the Volmer-Tafel mechanism or by the Volmer-Heyrowsky mechanism.[30d, 84] The first step is always the Volmer reaction which leads to an electron transfer.

$$H^+ + e^- \rightleftharpoons H_{ad}$$

The reaction of adsorbed hydrogen atom H_{ad} to molecular hydrogen follows at the electrode. This can happen either by the Tafel reaction

$$2\,H_{ad} \rightleftharpoons H_{2\,ad}$$

or by the Heyrowsky reaction

$$H^+ + H_{ad} + e^- \rightleftharpoons H_{2\ ad}$$

It is nearly impossible to experimentally distinguish between these two possible mechanisms.[30d] The is step is the desorption of the formed hydrogen:

$$H_{2\ ad} \rightleftharpoons H_2$$

The rate-determining step is of interest, it depends on the adsorption energy of the hydrogen atom. For a weak metal-hydrogen bond, like with mercury, the Volmer reaction is the slower step. With increasing the strength of the bond the Tafel or the Heyrowsky reaction determines the rate of reaction. The comparison of gold and silver shows that the latter has the weaker bond with atomic hydrogen.[85] The consequence is that on gold the desorption rate of hydrogen is lower. This is caused by the slower Tafel (or Heyrowsky) reaction that controls the release of the formed gas. On the silver electrode H_2 is immediately released after the slower Volmer reaction took place. The amount of molecular hydrogen should be controlled by the kinetics on gold, thus this should lead to smaller bubbles. This would coincide with the results found in chapter 4.1. An evolution-dissolution equilibrium exists on gold. This equilibrium might be affected by the changed kinetics on silver.

To investigate the influence of the electrode material, two different electrolytes in various concentrations were examined on silver and gold electrodes. One was potassium nitrate (Figure 20) the other was sodium nitrate (Figure 19).

For all electrolytes the frequency shifts are more significant with increasing concentration of the salt. It can clearly be seen that there are no negative frequency shifts at small negative potentials with the silver electrodes for both electrolytes. If the overpotential was the main influence, there should be a negative frequency shift. Decomposition potentials can differ from the ones observed with the gold electrode. The absence of negative shifts indicates that there are no nanobubbles. Hydrogen bubbles of macroscopic size are formed even at small negative potentials.

As mentioned above the kinetics of hydrogen evolution is changed due to the strength of the metal-hydrogen bond. Since the gold-hydrogen bond is stronger than the silver-

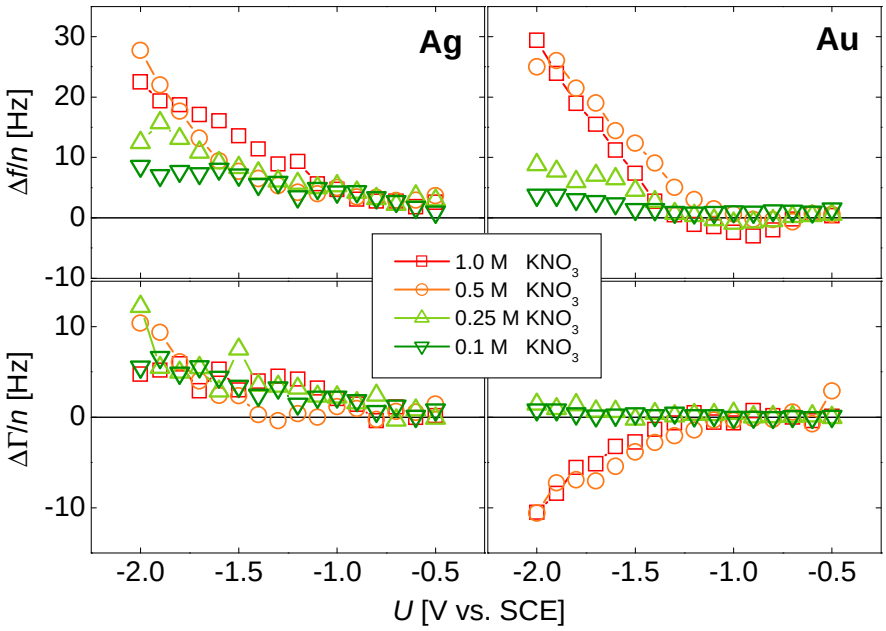

Figure 20: Frequency and bandwidth shifts on silver and gold electrodes with KNO_3 as electrolyte. On the left hand side the values for the silver electrode are depicted, for comparison the values for the gold electrode are shown on the right.

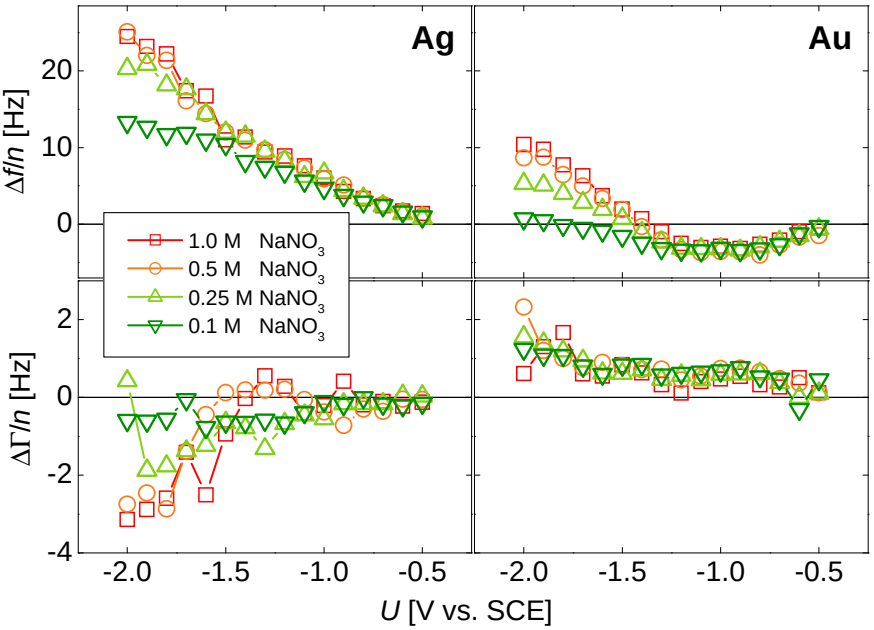

Figure 19: Frequency and bandwidth shifts on silver and gold electrodes with $NaNO_3$ as electrolyte. On the left hand side the values for the silver electrode are depicted, for comparison the values for the gold electrode are shown on the right.

hydrogen bond the Volmer reaction should be faster on gold. On silver the Tafel (or Heyrowsky) reaction proceeds with a higher rate. Due to the slower release of the molecular hydrogen on gold the formation of nanobubbles should be prefered. This

kinetic control is also the reason why there are nanobubbles at small negative potentials and macrobubbles at large negative potentials (see chapter 4.1). For the silver electrode the release of molecular hydrogen is more rapid hence resulting in bigger bubbles and only positive frequency shifts. The evolution-dissolution equilibrium is influenced by the changed kinetics. For silver electrode the evolution of hydrogen is a lot faster than the dissolution. This can be an explanation why there is no formation of nanobubbles on silver electrodes.

To summarize this chapter, with changing the electrode material the formation of nanobubbles is strongly influenced. A weak metal-hydrogen bond inhibits the formation of nanoscopic bubbles. This is caused by the higher rate of release for the formed H_2. When this rate is decreased compared to the rate on gold, the formation of nanobubbles should be enhanced. The assumed mechanism is supported by the fact that high negative potentials entail macroscopic bubbles and low negative potentials nanoscopic ones. To confirm these findings, other electrode materials should be used. As an alternative a metal with a very strong hydrogen bond (e.g. platinum or tungsten) could be modified by various amounts of mercury (very weak hydrogen bond) to form an amalgam.

4.5 Addition of Surfactant

Surfactants lead to a decrease of the surface tension caused by their amphiphilic character. As mentioned in chapter 4.1 and will be confirmed in chapter 6 by numerical means that the softness of the bubble determines the sign of the frequency shift. The softness describes the ability of the bubble to be deformed by the MHz shear field. It

Tergitol MIN FOAM 1X

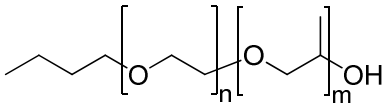

Lutensol AT50
n=15-17; m=50

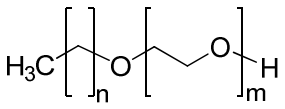

CTAB

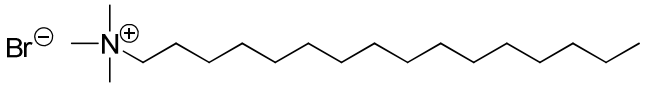

Figure 21: Chemical structures of the used surfactants.

depends on the Laplace pressure of the bubbles, therefore on surface tension and radius of curvature (Equation 8). If bubbles are stiff (nanoscopic size or high surface tension) the surrounding water is dragged along and negative frequency shifts are observed. When the bubbles are soft, which corresponds to large sizes or a low γ, the observed frequency shifts are positive. Addition of surfactants should lead to softer bubbles caused by their surface-active character which reduces the surface tension of the electrolyte. Due to their amphiplic nature they are enriched at surfaces. A change in sign of the frequency shift should be the effect of adding surfactant to the solution. There is a caveat though: In the simulations showed in the appendix, the surface tension was varied over a few decades. Such large variations cannot be achieved with surfactants. Surfactants lower the surface tension up to a factor of 10, but rarely more than that.

For the investigation of the influence on bubbles, three different types of surfactants were chosen, Lutensol AT50, Tergitol MIN FOAM 1X (both nonionic surfactants), and CTAB (cetyl trimethylammonium bromide, cationic surfactant). Chemical structures of the components are shown in Figure 21. The average frequency and bandwidth shifts are

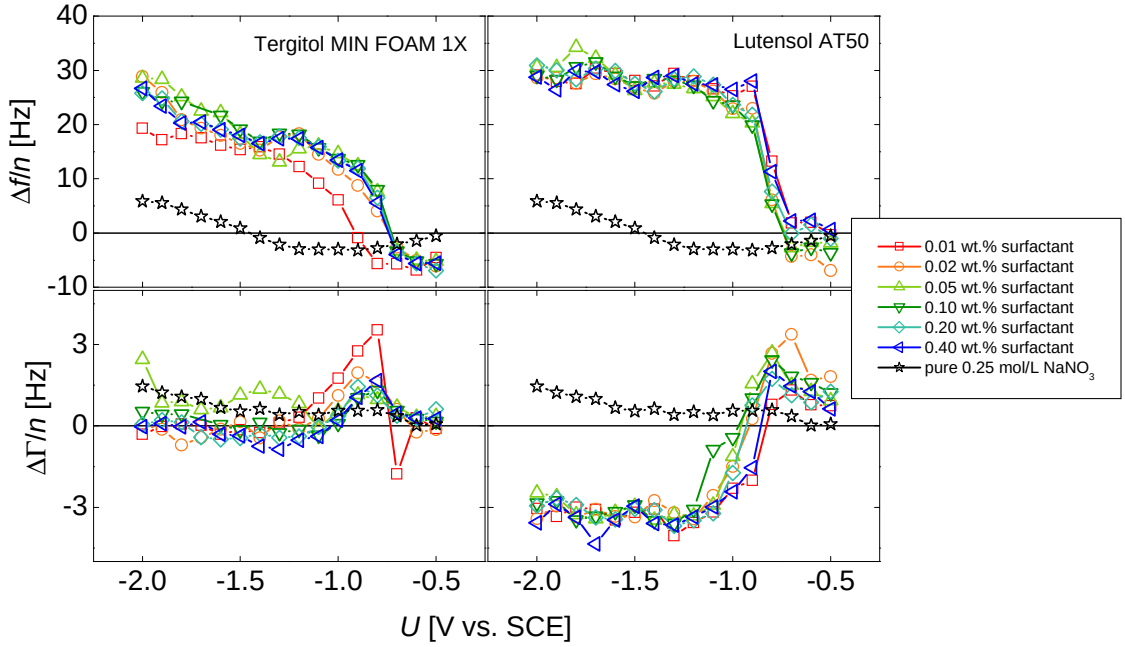

Figure 22: Average frequency and bandwidth shifts with 0.25 mol/L $NaNO_3$ with various surfactants. The average shifts observed with pure 0.25 mol/L $NaNO_3$ are shown as ★. Left panels: addition of Tergitol, right panels: with Lutensol AT50 added to the electrolyte.

depicted in Figure 22, the electrolyte was 0.25 mol/L $NaNO_3$. Anionic surfactants were not tested since they should be repelled by the front electrode of the QCM. Their charge is negative and the voltages applied at the WE are negative as well.

It is found that the two nonionic surfactants show similar frequency shifts. At small negative potentials they exhibit slight negative frequency shifts. They change abruptly to positive shifts with decreasing the voltage further. A dependence on the concentration of the surfactant is not found for the investigated range. The frequency shifts of the pure electrolyte shown in Figure 22 bear no resemblance to the frequency shifts found with these surfactants. It is possible that the initial negative frequency shifts are caused by adsorption of the surfactant on the electrode rather than nanobubbles. This adsorption, which also influences all obtained frequency shifts, can be observed in the time dependent Δf values (Figure 23). Frequency shifts caused by adsorption and those by bubbles interfere in these measurements. After the addition of the surfactant (arrows in Figure 23), Δf decreases rapidly. At this point no potential is applied. The initial decrease must be caused by the surfactant.

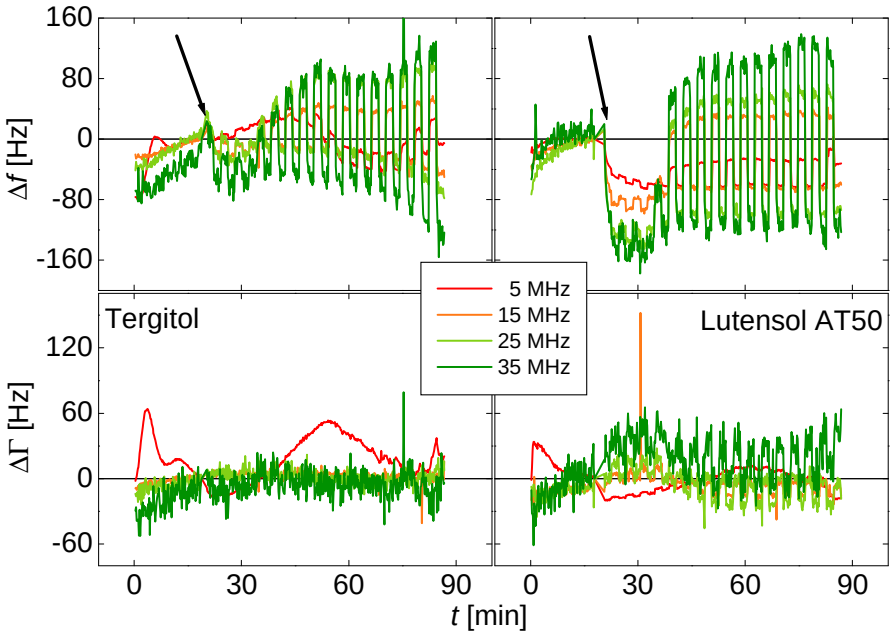

Figure 23: Typical observed time dependent frequency and bandwidth shifts for the two nonionic surfactants. The added amount of surfactant is 0.02 wt.% in 0.25 mol/L $NaNO_3$ solution. The arrow indicates the addition of the surfactant. After that the baseline of Δf drops which is an indicator for adsorption of the surfactant.

By increasing the negative potentials, hydrogen is formed and bubbles do not behave as stiff objects. Therefore they do not increase the hydrodynamic drag of the electrode. The bubbles decrease the coupled mass to the QCM. Positive frequency shifts are not only caused by an adsorption and desorption of the surfactant. This is supported by Figure 23. The observed shifts are positive hence a part of the positive shifts must result from soft or big bubbles. In the same potential range as the cross-over from negative to positive Δf, a step in the bandwidth shifts is observed as well. This step is small with Tergitol as added surfactant, and it is significant with Lutensol AT50. For the latter the shift in bandwidth refers to Kanazawa behavior, because of the reverse algebraic sign of frequency and bandwidth shift. The sample acts more viscous than the electrolyte with Tergitol. The measurements show that adsorption and desorption takes place. The adsorption can lead to a change in viscosity. This change might be reason for the different behavior in the bandwidth shift of the two surfactants. This leads to the conclusion that for Lutensol AT50 it is more likely that desorption of the surfactant takes place than for Tergitol.

These different shifts in bandwidth could also be caused by an additional effect of the hydrogen bubbles formed at the electrode. Gas above a QCM leads to narrow peaks in the impedance analysis. The change of the behavior caused by gaseous domains is more significant with Lutensol AT50. This surfactant leads to a higher coverage with gas at the electrode. This increased amount of hydrogen must be present in the volume where the QCM is sensitive.

For the cationic surfactant CTAB another developing of the frequency shifts is observed (Figure 24). At low negative potentials a slight and constant positive frequency shift was measured. When reaching about –1.3 V the trend of the values switches to the values obtained in measurements with the pure electrolyte. It is possible that the WE is totally blocked by adsorbed surfactant. No evolution of hydrogen took place. This ohmic polarization of the surface only occurs when a cationic surfactant is present, due to the negative potential of the electrode and the resulting coulomb interactions of electrode and molecules. When reaching a critical voltage, the surfactant is no longer able to block the

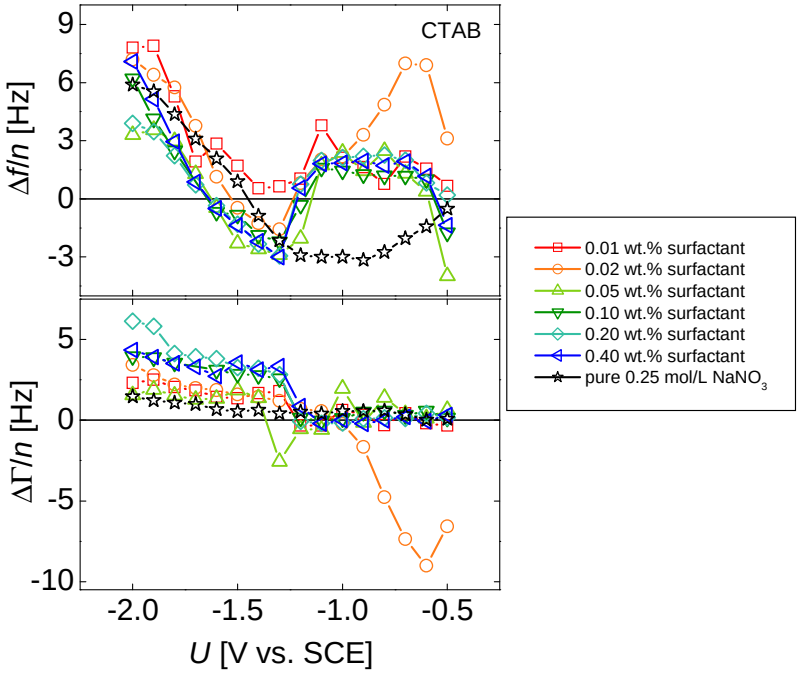

Figure 24: Time-averaged frequency and bandwidth shifts with CTAB as added surfactant. Main electrolyte was 0.25 mol/L $NaNO_3$. The average shifts observed with pure 0.25 mol/L $NaNO_3$ are shown as ★.

electrode and bubbles are formed. After this critical potential approximately the same frequency shifts as with pure sodium nitrate are obtained. The surfactant does not influence the frequency shifts at high negative potentials. This is not expected, because the surfactant should be enriched at the electrode and reduces the surface tension of the gas-liquid interface. Due to the negative potential of the electrode the cationic surfactant is strongly attracted by the surface. This should lead to a highly increased concentration in the vicinity of the surface. The surfactant is not enriched at the interface of the bubble. The interactions of the surfactant and the charged electrode are very strong. Therefore no surfactant is present at the gas-liquid interface. The slight positive frequency shifts at small negative potentials can be caused by the enriched surfactant. This enrichment changes the viscosity, respectively the density, in the vicinity of the electrode which influences the resonance frequency of the quartz crystal.

As a conclusion, surfactants lead to a change of Δf and $\Delta\Gamma$ relative to the pure electrolyte. These changes are more significant for Δf. They strongly depend on the nature of the surfactant. The interactions, especially with the electrode, are governed by

the headgroup's charge of the amphiphilic molecule. Nonionic surfactants showed ad- and desorption on the electrode with simultaneous formation of soft bubbles. The crossover between hard and soft bubbles happens at small negative voltages. This indicates that the lowered surface tension does influence the response of the QCM on bubble formation. For the cationic surfactant the Coulomb interactions of the positively charged headgroup and the negatively charged electrode are predominant. The cationic surfactant blocks the electrode hence formation of hydrogen bubbles is suppressed by an ohmic polarization. Only by increasing the negative potential, the evolution of H_2 can take place. Beneath this critical potential frequency shifts induced by the sample are like the ones observed in the experiments with pure electrolyte. The surfactant does not influence Δf even though it should reduce the surface tension of the gas liquid interface. It must be depleted at the gas-liquid interface and the surfactant is enriched directly at the electrode.

4.6 Variation of the Electrolyte

By varying the electrolyte the relationship of the Hofmeister series with bubble formation and properties of the bubbles should be examined. The Hofmeister series is linked to various phenomena in aqueous electrolytes.[75] It might influence the bubbles formed by electrochemical means. Since the effect of an ion on a system should not be considered without the counterion, anions were varied and the cation stayed the same. The latter was sodium in the experiments.

By comparing Δf and $\Delta\Gamma$ (Figure 25) for the electrolytes it is hard to quantify how well the values follow the Hofmeister series. For the concentrations of 0.25 mol/L, 0.5 mol/L and 1 mol/L no order can be found, but for the concentration of 0.1 mol/L one exists. Just one of the salts, $NaClO_4$, does not entail frequency and bandwidth shifts that fit into the order of the Hofmeister series. Only the smallest concentration of the electrolytes shows this correlation. The destabilizing salts lead to positive Δf and by changing from kosmotropic to chaotropic salts the frequency shifts decreases for the low electrolyte concentration. For $\Delta\Gamma$ the trend is reversed and lessened. The stabilizing salts facilitate the formation of nanobubbles that enhance the hydrodynamic drag at the interface which

leads to negative Δf. The destabilizing salts show only small positive frequency shifts. Those can be caused by big bubbles on the electrode of the crystal. The observed positive shifts are relatively small. They can be reduced by bubbles that detach from the surface. This detachment can be a result of the specific ion interactions.

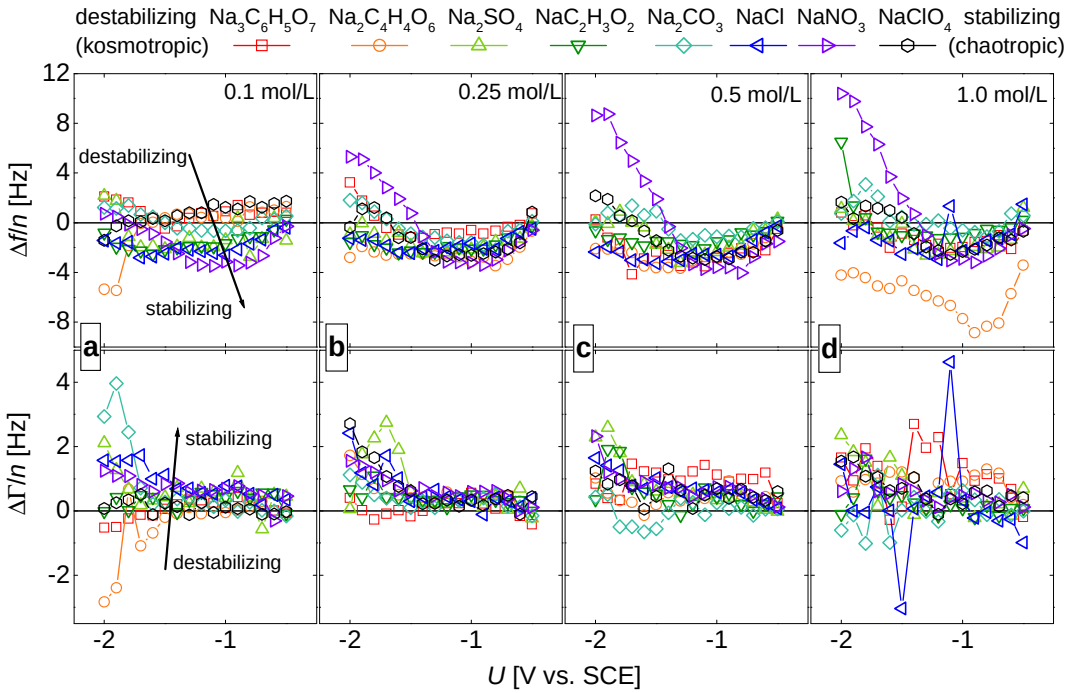

Figure 25: Frequency and bandwidth shifts for various sodium salts. The salts are ordered according to the Hofmeister series from the most destabilizing salt (□ sodium citrate) to the most stabilizing salt (⬡ sodium perchlorate). From panels a to d the concentration of the electrolyte increases from 0.1 mol/L over 0.25 mol/L and 0.5 mol/L to 1 mol/L. In panels b to d no order according to Hofmeister can be found. In panels a good order can be found for $\Delta f/n$ with exception of $NaClO_4$. This order is found for $\Delta\Gamma/n$ as well, but less obvious.

In Figure 26 the correlation to the Hofmeister series of the low electrolyte concentration is shown. The salts are ordered according to the Hofmeister series. It can be found that the salts show an effect that follows the Hofmeister series. Stabilizing salts lead to more negative frequency shifts than destabilizing salts. The error bars show that here reproducibility, which was mentioned in chapter 4.2, is a problem as well. But the chosen potentials show all the same trend. Only by further increase of the WE potential the order according to Hofmeister is lost.

Other possibilities that lead to small positive shifts are other geometries of the bubbles (see chapter 4.1).[39] As mentioned in chapter 2.3.1 there are reports on nanobubbles that

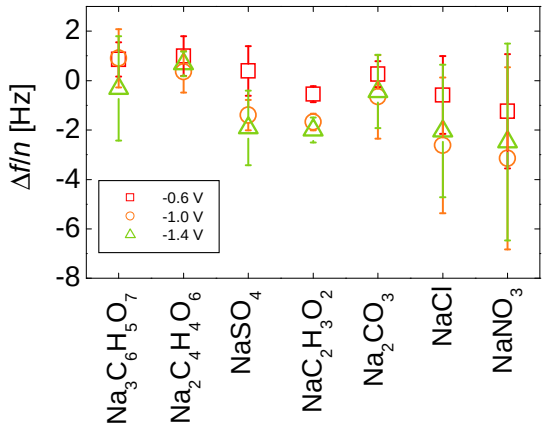

Figure 26: Frequency shifts of the 0.1 mol/L electrolytes. The salts are ordered according to the Hofmeister series. Left are the destabilizing salts and right are the stabilizing ones. Standard deviation is shown as error bars.

show positive Δf. The bubbles were very stable, were produced by solvent exchange method, and had large contact angles. When a bubble is shallow, it exhibits no hydrodynamic drag. The liquid can stream over the bubble and is not trapped in between bubbles. This case results in positive frequency shifts. The same is true for bubbles with small contact angles. Those bubbles in the shape of a truncated sphere can move on their position and do not enhance the hydrodynamic drag. Bubbles with high contact angles exhibit larger r than bubbles with small contact angles if the volumes are the same. Due to the higher Laplace pressure of the latter bubbles it is more likely that bubbles with a high contact angle are formed. Destabilizing salts therefore lead to shallow bubbles. This results in positive Δf of the QCM.

The order according to the Hofmeister series is lost when increasing the salt concentration (Figure 25). A reversal of the Hofmeister series following an increase of concentration was found by Robertson et al. in 1911.[78] This reversal does also happen in the present case. It is no perfect inversion. The good order with 0.1 mol/L electrolytes changes to no specific order with higher concentrations. It might be possible by further increase of the concentration of the electrolyte to obtain an order reverse to the one found for 0.1 mol/L electrolytes.

Schwierz et al. did molecular dynamics simulations on the Hofmeister series and investigated the phenomenon of the reversal of this order.[79] They showed that

depending on the surface polarity, surface charge, and on the concentration of the electrolyte the Hofmeister series could change. This reversal of the series can be either complete or partial. The order depends on the interactions of the ions with the surface, respectively the protein. In the present case the surface consist of two sections. One part of the interactions is governed by the gold electrode and the other is affected by the gas-liquid interface. The change in the Hofmeister series due to these interactions is less significant if the concentrations of the electrolytes are low.

One of the main problems of the Hofmeister series is that it cannot be quantified by one value. There are several attempts to put a value to the ion specific interactions.[80] The problem with all these parameters is that they mostly represent just one part of the occurring interactions. Since there is no other possibility to quantify the Hofmeister series some of these values were correlated to the observed response of the QCM. Values that were correlated to frequency and bandwidth shift are hydrodynamic radius,[86] Gaussian radius,[87] polarizability,[87] and surface tension increment.[81] With these a correlation coefficient ζ can be calculated.[88]

$$\zeta = \frac{\left\langle \left(x_i - \langle x \rangle\right) \cdot \left(y_i - \langle y \rangle\right) \right\rangle}{\sqrt{\left\langle \left(x_i - \langle x \rangle\right)^2 \right\rangle} \cdot \sqrt{\left\langle \left(y_i - \langle y \rangle\right)^2 \right\rangle}} \tag{18}$$

The triangular brackets denote the average. The variables *x* and *y* are totally uncorrelated when ζ = 0. When the ζ approaches 1 or –1 there is a perfect correlation of the two values. For *x* the values of the hydrodynamic radius, the Gaussian radius, the polarizability, or the surface tension increment were used. The *y* values are the measured data of Δf and $\Delta\Gamma$. The first three parameters for *x* are all a scale for the size of the anion which is varied in this set of experiments. The influence of the sodium cation is not considered in those correlations, because it is only possible to compare salts with the same cation. On the contrary the surface tension increment is a value that is determined for the whole salt and not for individual ions. This provides an opportunity not only to find a correlation with one type of salts, e.g. sodium salts, but also to include various salts, e.g. the comparison of various sodium salts with various potassium salts.

The correlation coefficient ζ is calculated for the surface tension increment twice. One is for the sodium salts (Figure 27 a and b) and the other with addition of other salts (Figure 27 c and d). The coefficient is determined for each potential. Therefore the dependency of the correlation coefficient on the applied voltage can be followed.

The correlation coefficient for the frequency and bandwidth shifts is closer to zero when the shifts of the potassium and ammonium salts (Figure 27 c and d) are added to the calculation. In those cases lower correlation can be found than for just the sodium salts. Especially at high potentials ζ drops to zero. This trend can be found for the correlation coefficient of the sodium salts for Δf (Figure 27 a) as well. For the pure sodium salts series better correlation was found. Even though ζ shows values near to 1 or –1 for $\zeta_{\Delta\Gamma}$ (Figure 27 b) they exhibit a large variability. The values are evenly distributed around zero, therefore only a small correlation to the surface tension increment could be found.

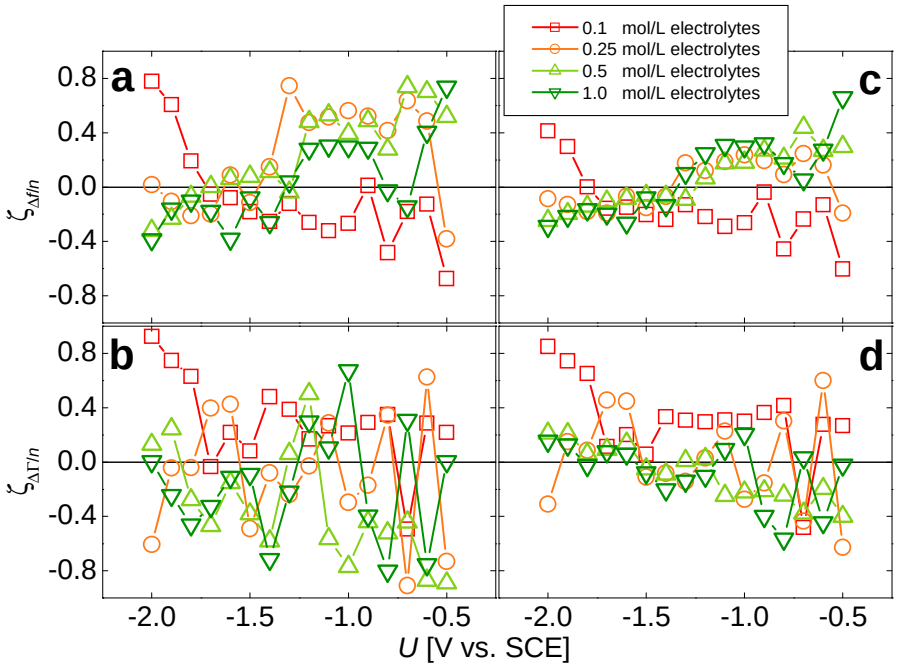

Figure 27: Correlation coefficient ζ for surface tension increment and Δf (a and c) or $\Delta\Gamma$ (b and d). The coefficient is calculated for the sodium salts ($NaNO_3$, Na_2SO_4, Na_2CO_3, $NaC_2H_3O_2$, $NaClO_4$, NaCl, panels a and b) and with additional salts (sodium salts plus NH_4NO_3, KCl, KNO_3, panels c and d). The correlation coefficient is given for the electrolytes in different concentrations as stated in the legend.

Since the surface tension increment is one of the factors that govern the Hofmeister series it was not expected to show such small ζ. The 0.1 mol/L electrolytes show the least correlation, this is even more unexpected, because a Hofmeister series could be found for

these (Figure 25). For the mid range (0.25 mol/L and 0.5 mol/L) ζ is good at low potentials which correspond to formation of nanobubbles. Nanobubbles should be influenced by increased surface tension. According to the Laplace equation (8) the stiffness of the bubble increases by increasing the surface tension. As a consequence the frequency shift should decrease. The correlation is best for the potential regime of the nanobubbles, but it is not significant. The effect on the difference in surface tension is too small to govern the response of the QCM.

Other correlations were calculated for the sizes of the anion, expressed by the hydrodynamic radius, Gaussian radius, and the polarizability (Figure 28). The determined ζ of those in general is higher than the ones for the surface tension increment and it shows clear trends. The correlation is good but not perfect. It depends on the

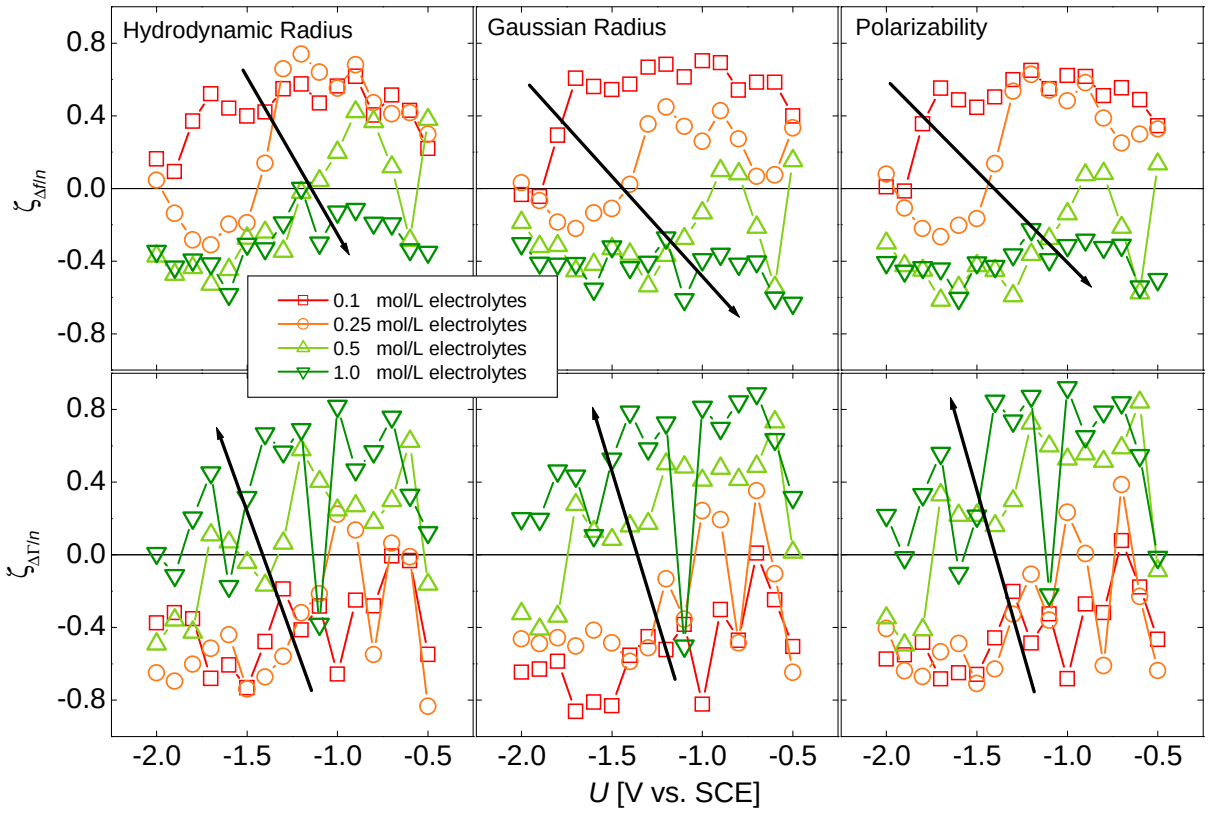

Figure 28: Correlation coefficients for anion sizes with Δf (upper panels) and $\Delta\Gamma$ (lower panels). The different concentrations of the electrolytes are indicated in the legend. A development from high to low $\zeta_{\Delta f}$ can be found for all anion sizes. For the correlation coefficient with $\Delta\Gamma$ the trend is reverse. For the correlation the frequency and bandwidth shifts of $NaNO_3$, NaCl, $NaClO_4$, $NaC_2H_3O_2$, Na_2SO_4, Na_2CO_3, $Na_2C_4H_4O_6$, and $Na_3C_6H_5O_7$ were used.

concentration of the electrolytes. The dependence indicates an inversion of the influences on the change of the amount of salt.

The correlation coefficient for the frequency shift $\zeta_{\Delta f}$ becomes smaller when the concentration is increased. With increasing the concentration this drop can be observed at high negative voltages. The correlation changes its sign. The absolute values for $\zeta_{\Delta f}$ are smaller for higher concentrations. This is in accordance with the results found for the Hofmeister series. The low electrolyte concentration shows the best agreement with the theory. A switch of the order can be found as well. Negative frequency shifts are observed when the anion is small. Those enhance the formation of nanobubbles when the concentration is low. For high concentrations big anions, like citrate, tartrate, and sulfate do induce nanobubbles that lead to negative frequency shifts. In those cases ζ is negative.

Another possible explanation that includes both correlation regimes is that small anions favor the formation of hydrogen in general. When the concentration of the electrolyte is low the evolution of hydrogen is hindered due to the lower conductivity of the electrolyte. The formation of nanobubbles is preferred for all electrolytes. When the small anions lead to formation of more hydrogen than the bigger anions, more nanobubbles are formed on the electrode of the QCM. They do not form macroscopic bubbles due to kinetic reasons (see chapter 4.1 and 4.4). The water between the bubbles is dragged along more efficiently and Δf is smaller. By increasing the concentration of the electrolyte the resistance of the electrolyte is reduced. More hydrogen can be formed hence macrobubbles arise at the cathode. Since small anions enhance the evolution of H_2, bigger bubbles are formed, and as a result Δf is increased because big bubbles reduce the coupled mass.

The observed reversal of the correlation coefficient at high potentials is hard to interpret, because the absolute values obtained for ζ are smaller than those for small negative potentials. This shows that the relation between the anion size and the frequency shift is not as strong as at small negative potentials. These developments can be found for all correlation coefficients of the anion sizes.

For $\zeta_{\Delta\Gamma}$ the trend is reverse to $\zeta_{\Delta f}$. For low electrolyte concentrations with a small anion $\Delta\Gamma$ is high. Small anions entail more dissipation at low electrolyte concentrations. Since small anions enhance the formation of nanobubbles, as stated above, the result seems contradictory to the other results found in this work. When bubbles are small enough they exhibit stiffness due to the change of their internal pressure upon deformation (Figure 11). Therefore nanobubbles should entail less dissipation than macroscopic bubbles. In the examined systems mostly no or only a small changes in $\Delta\Gamma$ were observed. The small difference between the cases, where nanobubble formation is enhanced and the ones with favored formation of macrobubbles, is the fraction of the surface covered with gas. This fraction should be higher for bigger bubbles, especially if the penetration depth of the shear wave is taken into account. Nanobubbles can be smaller than $\delta/2$. Gas shows less dissipation than liquids. A reduction of the bandwidth occurs if the sample on the quartz consists of more gas. Based on these small bandwidth shifts the difference of the effective fraction of gas must be small, that contributes to the QCM's signal.

When changing to high concentrations $\zeta_{\Delta\Gamma}$ switches its sign which corresponds to the development of the correlation coefficient of Δf. The small anions now induce less dissipation than the bigger ones. The reduction of dissipation is caused by a higher amount of gas at the surface of the QCM. It is in agreement with the statements given above, the formation of bigger bubbles is preferred if the anions are small.

In summary, the investigation of the anion dependent response of the quartz crystal showed that a Hofmeister series could be found. This is restricted to small concentrations. No order according to the Hofmeister series exists when the concentration is increased. There is a correlation of Δf and $\Delta\Gamma$ with various anion sizes and slight dependence on the surface tension increment was found. Small anions enhance the formation of nanobubbles at low salt concentration. With high amounts of salts big anions lead to nanobubbles. Those factors seem to govern the formation of nanobubbles. By addition of more salt the formation of macroscopic bubbles is supported.

4.7 Variation of Concentration

When examining the frequency shifts of the same electrolyte with different concentrations, various developments could be found (Figure 29). This concentration dependence is discussed just phenomenological. Some salts lead to strong concentration dependence of Δf, e.g. sodium nitrate (Figure 29 a). The nitrates ($NaNO_3$, NH_4NO_3, KNO_3) and sodium tartrate showed this strong dependence, therefore the amount of the added electrolyte has an influence on the reaction at the electrode as well as the kind of salt. The trend of the influence differs. Increase of the concentration can either lead to increase of the frequency shift or to a decrease. The reasons for this are unclear why there is a dependence.

For other salts no effect was found on the change of the concentration (Figure 29 b). This was found for NaCl, Na_2SO_4, and $NaClO_4$. Those electrolytes just influence the formation of bubbles just by their kind. The last issue of concentration dependence is a nonlinearity of the frequency shifts like in Figure 29 c. The difference to electrolytes that are represented by Figure 29 a is that Δf does not just increase or decrease by increasing the amount of electrolyte. This behavior was shown by sodium carbonate, sodium acetate, and sodium citrate.

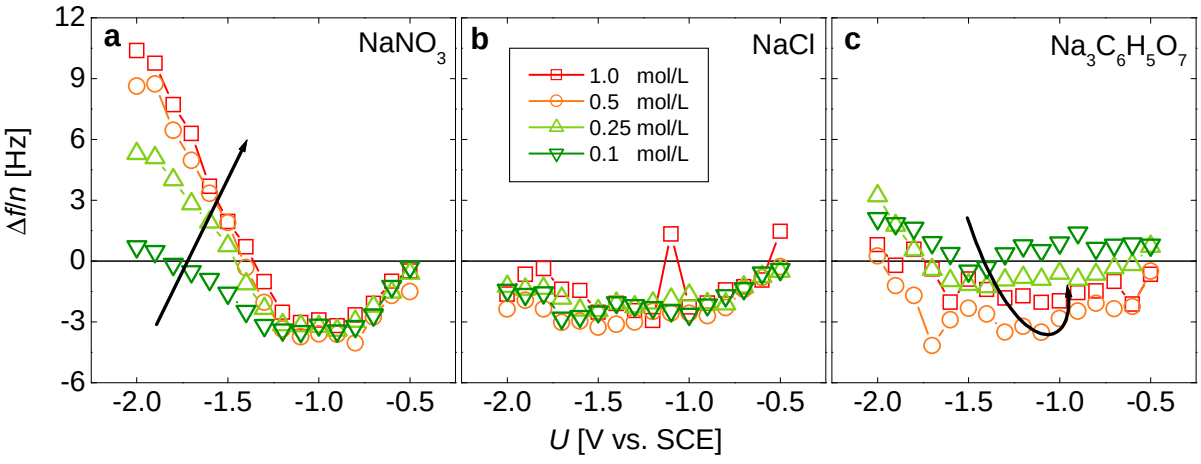

Figure 29: Exemplary frequency shifts with concentration dependence. Arrows indicate the change of Δf upon increasing the concentration. **a**: Δf for different concentrations of $NaNO_3$, by increasing the amount of electrolyte the frequency increases. **b**: frequency shift is independent of concentration of the electrolyte NaCl. **c**: nonlinear dependence of Δf on the concentration of the electrolyte, here shown for sodium citrate.

It is not clear why the salts exhibit these dependencies. The salts can not be arranged in groups like inorganic/organic ions or monovalent/bivalent ions, they do not follow the Hofmeister series, and they are not ordered according to their acidity. The effect exists but no explanation could be found. The concentration dependence of the formation of bubbles still needs investigation, especially with salts of other cations. Perhaps the most important influence factor is the anion, as it can be found for the nitrates.

5 Conclusion

This thesis dealt with the influences of various experimental parameters on the formation and the properties of hydrogen bubbles. These were produced electrochemically. For monitoring the changes at the electrode, a quartz crystal microbalance was used as the working electrode in a three-electrode setup.

The properties (the size, in particular) of the bubbles were primarily influenced by the applied potential. Other factors like the supporting electrolyte, the electrode material, dissolved carbon dioxide, and added surfactants were investigated, as well.

Decomposition of water leads to the evolution of hydrogen at the cathode. Hydrogen forms surface-attached bubbles whose sizes depend on the applied voltage. The response of a quartz crystal microbalance to the formation of bubbles varies, depending on the size of the bubbles. At small negative potentials nanobubbles are formed. These lead to negative frequency shifts. In this case, the mass coupled to the crystal is increased by trapped water. The formed nanobubbles are in an evolution-dissolution equilibrium. They are not stable. Nanobubbles do not behave soft; to the surrounding water they seem like bricks. The normal forces onto the air-water interface induced by deformation are so large that deformation is unfavorable. The hydrodynamic drag is increased by nanobubbles. They do not lead to slip although they exhibit a lower density than water. The overtone dependence of frequency and bandwidth shifts is the same as for Sauerbrey films.

When bubbles grow bigger they become soft. Their Laplace pressure is smaller, and therefore the deformation-induced normal forces are lower as well. The macrobubbles can be deformed by the surrounding water. The resonance frequency of the crystal increases, because the coupled mass on the quartz is reduced. The fraction of gas now determines the QCM signal. Those bubbles lead to slip. Simulations with Finite Element Methode (FEM) support this interpretation. They showed that small, respectively stiff bubbles lead to negative frequency shifts of the QCM. Those exhibit an overtone dependence according to Sauerbrey that was also found in the experiments. The shifts in bandwidth, $\Delta\Gamma$, were smaller than Δf in all the conducted experiments. This is also

supported by the FEM simulation. Because $\Delta\Gamma$ is small, the data analysis here mostly relies on Δf.

The rate of hydrogen formation (which depends on the overpotential and pH) is expected to be one of the parameters determining the number and the size of the gas bubbles. A second, more difficult parameter is the likelihood of bubble nucleation. Supersaturation of dissolved gas does not immediately lead to bubble formation. Once formed, bubbles may or may not grow in size due to Ostwald ripening.

Various factors influencing nanobubble formation were investigated:

- *Cleaning of electrolyte and electrode*

It is obvious that the surface structure influences the nucleation process of nanobubbles. Therefore best reproducibility was obtained by employing of identical crystals in repeated experiments. Bubbling nitrogen through the solution and electrochemical cleaning also improved the reproducibility. Purging with nitrogen is crucial to obtain reliable results.

- *Addition of carbondioxide*

More negative frequency shifts were found when CO_2 was dissolved in the electrolyte. *Dissolved carbon dioxide facilitates the formation of nanobubbles.* Presumably, this is induced by preformed gas bubbles of CO_2 that act as nucleation sites.

- *Comparison of gold and silver as electrode materials*

On silver electrodes nanobubbles are no longer formed. The silver-hydrogen bond is weaker than the gold-hydrogen bond. With silver as the electrode material, desorption of molecular hydrogen from the electrode is easier than with gold. This influences the formation mechanism in a way that only macrobubbles can develop.

- *Addition of surfactant*

The influence of surfactants depends on their nature. *Nonionic surfactants show adsorption-desorption kinetics which interfere with the frequency shifts obtained from the bubble formation*. The frequency shifts show predominantly positive values. *For the*

studied cationic surfactant an ohmic polarization of the electrode at small negative potentials was observed. A critical voltage is needed to observe frequency shifts that are similar to the ones obtained without surfactant. The interactions of the positively charged surfactant and the negatively charged electrode determine the response of the QCM.

- *Variation of electrolytes*

Anions of the electrolyte were varied covering the Hofmeister series. *An ordering according to the Hofmeister series was found for low electrolyte concentrations of sodium salts.* As the amount of salt is increased a partial inversion of the Hofmeister series takes place. *No correlation was found for high electrolyte concentrations.*

Correlations to the surface tension increment, the hydrodynamic radius, the Gaussian radius, and the polarizability were determined. For those the *correlation coefficients were best with low salt concentrations* with the exception of the surface tension increment. The correlation coefficients change sign when increasing the concentration. This change is in agreement with the results of the Hofmeister series.

It could be shown that *nanoscopic bubbles exhibit properties which differ from those of macrobubbles*. Nanobubbles are stiff objects that enhance the hydrodynamic drag of a surface. Influences on the formation of nanobubbles via electrochemical means are various. The formation is governed by the electrochemically induced evolution of hydrogen and nucleation of the gas cavities with their subsequent growth. This work showed results which should lead to a deeper understanding of nanobubbles. It is important to do further research to understand the interplay of hydrogen formation, nucleation and Ostwald ripening.

6 Appendix: Finite Element Method for Modeling QCM

Finite Element Method (FEM) simulations were carried out to determine the frequency shift induced by nanobubbles on a QCM.[39] Those were done by D. Johannsmann. For detailed backgrounds on FEM simulations see Ref. 24. Just a review is given on the results for the special case of small bubbles on the crystal. The results are mentioned here to support the experimental findings of this thesis.

The FEM simulations were carried out with the Incompressible Navier-Stokes module by COMSOL (Göttingen, Germany). This can solve the (Navier-)Stokes equation for a given geometry. The FEM simulation lead to the shear stress at the quartz crystal surface. With that the load impedance Z_L can be determined which is needed to solve the Small Load Approximation (SLA, eq. 6). With the solution of the SLA frequency and bandwidth shifts can be determined.

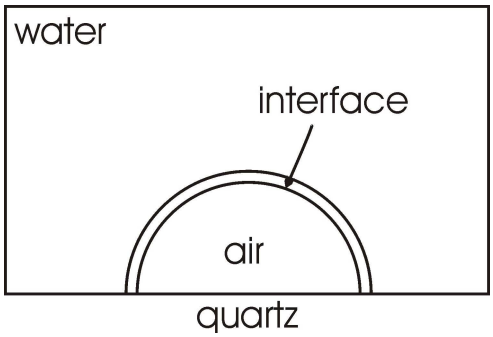

Figure 30: Schematic geometry of the FEM simulation. Properties of the indicated materials are assigned to those areas. The surface tension of the interface was incorporated via body forces.

The geometry that was used for the FEM simulation is given in Figure 30. It consists of a cell whose bottom oscillates tangentially. The bottom is equivalent to a quartz crystal. On this bottom a hemisphere is placed that stands for the gas phase. A second hemisphere is introduced and the space in between the two is the air water interface. Surface tension was incorporated into this space via body forces. This is necessary to simulate the gas-liquid interface. The rest of the cell exhibits the properties of water. Periodic boundary conditions are applied to both sides of the cell. For further explanations of the method and input values see ref. 39.

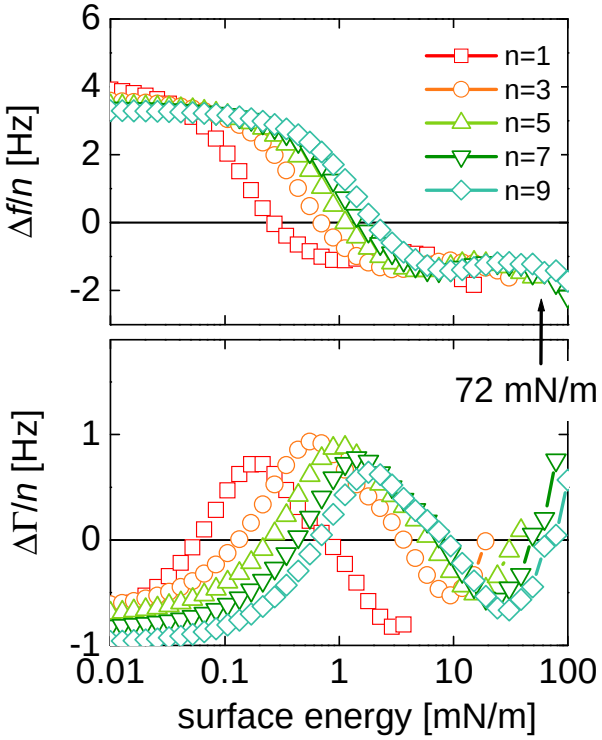

Figure 31: Resulting frequency and bandwidth shift of the FEM simulations for a hemispherical bubble. The shifts were calculated for different overtones of a crystal with 5 MHz as fundamental frequency. The arrow indicates the surface tension of water (72 mN/m).

With varying the surface tension of the interface the problem could be investigated over a big range of bubble sizes. This is possible because via the Laplace equation (8) the radius of curvature and the surface tension are linked. For a hemispherical bubble with a radius of 10 nm the frequency and bandwidth shifts shown in Figure 31 were calculated. The fraction of coverage with gas was about 2.5 %. For surface tensions in the order of γ for water negative Δf are obtained. When decreasing the surface tension which corresponds to an increased radius of curvature, the frequency shift changes its sign and becomes positive. These results are in agreement with the experimental results. The Sauerbrey scaling ($\Delta f \propto n$) stated in chapter 4.1 can be found in the results of the FEM simulation. The obtained shifts in bandwidth are smaller than Δf and behave more complicated.

The FEM simulations by D. Johannsmann lead to similar results as the experiments. They support the theory that small bubbles do behave like a surface roughness therefore decreasing the resonance frequency of the quartz crystal. Other geometries than a

hemispherical bubble are covered in ref. 39. Those do not lead to negative frequency shifts. Shallow bubbles and bubbles in the shape of a truncated sphere result in positive Δf.[40]

7 Literature

1. Parker, J. L.; Claesson, P. M.; Attard, P., Bubbles, Cavities, and the Long-Ranged Attraction between Hydrophobic Surfaces. *Journal of Physical Chemistry* **1994,** 98, (34), 8468-8480.

2. Lou, S. T.; Ouyang, Z. Q.; Zhang, Y.; Li, X. J.; Hu, J.; Li, M. Q.; Yang, F. J., Nanobubbles on solid surface imaged by atomic force microscopy. *Journal of Vacuum Science & Technology B* **2000,** 18, (5), 2573-2575.

3. Song, B.; Walczyk, W.; Schoenherr, H., Contact Angles of Surface Nanobubbles on Mixed Self-Assembled Monolayers with Systematically Varied Macroscopic Wettability by Atomic Force Microscopy. *Langmuir* **2011,** 27, (13), 8223-8232.

4. Steinem, C.; Janshoff, A., *Piezoelectric Sensors*. Springer: Berlin, Heidelberg, New York, 2007; Vol. 5. a: p. 173-210; b: p. 122; c: p. 123; d: p. 27-45.

5. Craig, V. S. J., Very small bubbles at surfaces-the nanobubble puzzle. *Soft Matter* **2011,** 7, (1), 40-48.

6. Ballantine, D. S.; White, R. M.; Martin, S. J.; Ricco, A. J.; Zellers, E. T.; Frye, G. C.; Wohltjen, H., *Acoustic Wave Sensors: Theory, Design, and Physico-Chemical Application*. Academic Press: San Diego, Boston, London, 1997. a: p. 70-139.

7. Ward, M. D.; Buttry, D. A., Insitu Interfacial Mass Detection with Piezoelectric Transducers. *Science* **1990,** 249, (4972), 1000-1007.

8. Marx, K. A., Quartz crystal microbalance: A useful tool for studying thin polymer films and complex biomolecular systems at the solution-surface interface. *Biomacromolecules* **2003,** 4, (5), 1099-1120.

9. Reuber, J.; Reinhardt, H.; Johannsmann, D., Formation of surface-attached responsive gel layers via electrochemically induced free-radical polymerization. *Langmuir* **2006,** 22, (7), 3362-3367.

10. Naumann, R.; Schiller, S. M.; Giess, F.; Grohe, B.; Hartman, K. B.; Karcher, I.; Koper, I.; Lubben, J.; Vasilev, K.; Knoll, W., Tethered lipid bilayers on ultraflat gold surfaces. *Langmuir* **2003,** 19, (13), 5435-5443.

11. Reviakine, I.; Rossetti, F. F.; Morozov, A. N.; Textor, M., Investigating the properties of supported vesicular layers on titanium dioxide by quartz crystal microbalance with dissipation measurements. *Journal of Chemical Physics* **2005,** 122, (20), 8.

12. Janshoff, A.; Galla, H. J.; Steinem, C., Piezoelectric mass-sensing devices as biosensors - An alternative to optical biosensors? *Angewandte Chemie-International Edition* **2000,** 39, (22), 4004-4032.

13. Saitakis, M.; Gizeli, E., Acoustic sensors as a biophysical tool for probing cell attachment and cell/surface interactions. *Cellular and Molecular Life Sciences* **2012,** 69, (3), 357-371.

14. Becker, B.; Cooper, M. A., A survey of the 2006-2009 quartz crystal microbalance biosensor literature. *Journal of Molecular Recognition* **2011,** 24, (5), 754-787.

15. Johannsmann, D., Viscoelastic, mechanical, and dielectric measurements on complex samples with the quartz crystal microbalance. *Physical Chemistry Chemical Physics* **2008,** 10, (31), 4516-4534.

16. Schumacher, R., Die Schwingquarzmethode. *Chemie in unserer Zeit* **1999,** 33, (5), 268-278.

17. Sauerbrey, G., Verwendung von Schwingquarzen zur Wägung dünner Schichten und zur Mikrowägung. *Zeitschrift für Physik* **1959,** 155, (2), 206-222.

18. Rodahl, M.; Kasemo, B., On the measurement of thin liquid overlayers with the quartz-crystal microbalance. *Sensors and Actuators a-Physical* **1996,** 54, (1-3), 448-456.

19. Johannsmann, D., Viscoelastic analysis of organic thin films on quartz resonators. *Macromolecular Chemistry and Physics* **1999,** 200, (3), 501-516.

20. Konash, P. L.; Bastiaans, G. J., Piezoelectric-Crystals as Detectors in Liquid-Chromatography. *Analytical Chemistry* **1980,** 52, (12), 1929-1931.

21. Kanazawa, K. K.; Gordon, J. G., The Oscillation Frequency of a Quartz Resonator in Contact with a Liquid. *Analytica Chimica Acta* **1985,** 175, (SEP), 99-105.

22. Schumacher, R., The Quartz Microbalance - a Novel-Approach to the Insitu Investigation of Interfacial Phenomena at the Solid Liquid Junction. *Angewandte Chemie-International Edition in English* **1990,** 29, (4), 329-343.

23. Bruckenstein, S.; Shay, M., An Insitu Weighing Study of the Mechanism for the Formation of the Adsorbed Oxygen Monolayer at a Gold Electrode. *Journal of Electroanalytical Chemistry* **1985,** 188, (1-2), 131-136.

24. Johannsmann, D.; Reviakine, I.; Rojas, E.; Gallego, M., Effect of Sample Heterogeneity on the Interpretation of QCM(-D) Data: Comparison of Combined Quartz Crystal Microbalance/Atomic Force Microscopy Measurements with Finite Element Method Modeling. *Analytical Chemistry* **2008,** 80, (23), 8891-8899.

25. Neubig, B.; Briese, W., *Das große Quarzkochbuch: Quarze, Quarzoszillatoren, Quarz- und Oberflächenwellenfilter (SAW), Messtechnik*. Franzis-Verlag: Feldkirchen, 1997; p. 221-291.

26. Beck, R.; Pittermann, U.; Weil, K. G., Impedance Analysis of Quartz Oscillators, Contacted on One Side with a Liquid. *Berichte Der Bunsen-Gesellschaft-Physical Chemistry Chemical Physics* **1988,** 92, (11), 1363-1368.

27. Rodahl, M.; Kasemo, B., A simple setup to simultaneously measure the resonant frequency and the absolute dissipation factor of a quartz crystal microbalance. *Review of Scientific Instruments* **1996,** 67, (9), 3238-3241.

28. Li, F. B.; Hillman, A. R.; Lubetkin, S. D.; Roberts, D. J., Electrochemical Quartz Crystal Microbalance Studies of Potentiodynamic Electrolysis of Aqueous Chloride Solution - Surface Processes and Evolution of H_2 and Cl_2 Gas-Bubbles. *Journal of Electroanalytical Chemistry* **1992,** 335, (1-2), 345-362.

29. Pletcher, D.; Greef, R.; Peat, R.; Peter, L. M.; Robinson, J., *Instrumental Methods in Electrochemistry*. Horwood Publishing: Chichester, 2001.

30. Hamann, C. H.; Vielstich, W., *Elektrochemie*. 3 ed.; Wiley-VCH: Weinheim, New York, Chichester, 2004. a: p. 236-237; b: p. 69; c: p. 91; d: p. 334-338.

31. Wedler, G., *Lehrbuch der Physikalischen Chemie*. 4 ed.; Wiley-VCH: Weinheim, 1997; p. 413-421.

32. Atkins, P. W., *Physikalische Chemie*. 1 ed.; VCH: Weinheim, Cambridge, New York, 1988; p. 159.

33. Ishida, N.; Inoue, T.; Miyahara, M.; Higashitani, K., Nano bubbles on a hydrophobic surface in water observed by tapping-mode atomic force microscopy. *Langmuir* **2000,** 16, (16), 6377-6380.

34. Seddon, J. R. T.; Lohse, D., Nanobubbles and micropancakes: gaseous domains on immersed substrates. *Journal of Physics-Condensed Matter* **2011,** 23, (13), 22.

35. Hampton, M. A.; Nguyen, A. V., Nanobubbles and the nanobubble bridging capillary force. *Advances in Colloid and Interface Science* **2010,** 154, (1-2), 30-55.

36. Binnig, G.; Quate, C. F.; Gerber, C., Atomic Force Microscope. *Physical Review Letters* **1986,** 56, (9), 930-933.

37. Zhong, Q.; Inniss, D.; Kjoller, K.; Elings, V. B., Fractured Polymer Silica Fiber Surface Studied by Tapping Mode Atomic-Force Microscopy. *Surface Science* **1993,** 290, (1-2), L688-L692.

38. Zhang, X. H.; Quinn, A.; Ducker, W. A., Nanobubbles at the interface between water and a hydrophobic solid. *Langmuir* **2008,** 24, (9), 4756-4764.

39. Finger, A.; Johannsmann, D., Hemispherical nanobubbles reduce interfacial slippage in simple liquids. *Physical Chemistry Chemical Physics* **2011,** 13, (40), 18015-18022.

40. Zhang, X. H., Quartz crystal microbalance study of the interfacial nanobubbles. *Physical Chemistry Chemical Physics* **2008,** 10, (45), 6842-6848.

41. Tsionsky, V.; Kaverin, A.; Daikhin, L.; Katz, G.; Gileadi, E., An experimental verification of the possible influence of gas nano-bubbles on the response of an electrochemical quartz crystal microbalance. *Physical Chemistry Chemical Physics* **2005,** 7, (8), 1830-1835.

42. Liu, G.; Wu, Z.; Craig, V. S. J., Cleaning of Protein-Coated Surfaces Using Nanobubbles: An Investigation Using a Quartz Crystal Microbalance. *Journal of Physical Chemistry C* **2008,** 112, (43), 16748-16753.

43. Seo, H.; Yoo, M.; Jeon, S., Influence of nanobubbles on the adsorption of nanoparticles. *Langmuir* **2007,** 23, (4), 1623-1625.

44. Zhang, X. H.; Maeda, N.; Craig, V. S. J., Physical properties of nanobubbles on hydrophobic surfaces in water and aqueous solutions. *Langmuir* **2006,** 22, (11), 5025-5035.

45. van Limbeek, M. A. J.; Seddon, J. R. T., Surface Nanobubbles as a Function of Gas Type. *Langmuir* **2011,** 27, (14), 8694-8699.

46. Zhang, X. H.; Ducker, W., Formation of interfacial nanodroplets through changes in solvent quality. *Langmuir* **2007,** 23, (25), 12478-12480.

47. Zhang, L. J.; Zhang, Y.; Zhang, X. H.; Li, Z. X.; Shen, G. X.; Ye, M.; Fan, C. H.; Fang, H. P.; Hu, J., Electrochemically controlled formation and growth of hydrogen nanobubbles. *Langmuir* **2006,** 22, (19), 8109-8113.

48. Yang, S.; Tsai, P.; Kooij, E. S.; Prosperetti, A.; Zandvliet, H. J. W.; Lohse, D., Electrolytically Generated Nanobubbles on Highly Orientated Pyrolytic Graphite Surfaces. *Langmuir* **2009,** 25, (3), 1466-1474.

49. Yang, S. J.; Dammer, S. M.; Bremond, N.; Zandvliet, H. J. W.; Kooij, E. S.; Lohse, D., Characterization of nanobubbles on hydrophobic surfaces in water. *Langmuir* **2007,** 23, (13), 7072-7077.

50. Hampton, M. A.; Donose, B. C.; Nguyen, A. V., Effect of alcohol-water exchange and surface scanning on nanobubbles and the attraction between hydrophobic surfaces. *Journal of Colloid and Interface Science* **2008,** 325, (1), 267-274.

51. Seddon, J. R. T.; Kooij, E. S.; Poelsema, B.; Zandvliet, H. J. W.; Lohse, D., Surface Bubble Nucleation Stability. *Physical Review Letters* **2011,** 106, (5), 4.

52. Brenner, M. P.; Lohse, D., Dynamic Equilibrium Mechanism for Surface Nanobubble Stabilization. *Physical Review Letters* **2008,** 101, (21), 4.

53. Ducker, W. A., Contact Angle and Stability of Interfacial Nanobubbles. *Langmuir* **2009,** 25, (16), 8907-8910.

54. Carr, M. W.; Hillman, A. R.; Lubetkin, S. D.; Swann, M. J., Detection of Electrolytically Generated Bubbles Using an Electrochemical Quartz Crystal Microbalance. *Journal of Electroanalytical Chemistry* **1989,** 267, (1-2), 313-320.

55. Liu, G.; Craig, V. S. J., Improved Cleaning of Hydrophilic Protein-Coated Surfaces using the Combination of Nanobubbles and SDS. *ACS Applied Materials & Interfaces* **2009,** 1, (2), 481-487.

56. Yang, J.; Duan, J.; Fornasiero, D.; Ralston, J., Kinetics of CO_2 nanobubble formation at the solid/water interface. *Physical Chemistry Chemical Physics* **2007,** 9, (48), 6327-6332.

57. Batchleor, G. K., *An Introduction to Fluid Dynamics*. 1 ed.; Cambridge University Press: Cambridge, New York, 2000; p. 148-150.

58. Neto, C.; Evans, D. R.; Bonaccurso, E.; Butt, H. J.; Craig, V. S. J., Boundary slip in Newtonian liquids: a review of experimental studies. *Reports on Progress in Physics* **2005,** 68, (12), 2859-2897.

59. Larson, R. G., *The Structure and Rheology of Complex Fluids*. 1 ed.; Oxford University Press: New York, Oxford, 1999.

60. Brochard, F.; de Gennes, P. G., Shear-Dependent Slippage at a Polymer Solid Interface. *Langmuir* **1992,** 8, (12), 3033-3037.

61. Meinhart, C. D.; Wereley, S. T.; Santiago, J. G., PIV measurements of a microchannel flow. *Experiments in Fluids* **1999,** 27, (5), 414-419.

62. Yamada, J., Evanescent wave Doppler velocimetry for a wall's near field. *Applied Physics Letters* **1999,** 75, (12), 1805-1806.

63. Pit, R.; Hervet, H.; Leger, L., Friction and slip of a simple liquid at a solid surface. *Tribology Letters* **1999,** 7, (2-3), 147-152.

64. Baudry, J.; Charlaix, E.; Tonck, A.; Mazuyer, D., Experimental evidence for a large slip effect at a nonwetting fluid-solid interface. *Langmuir* **2001,** 17, (17), 5232-5236.

65. Sun, G. X.; Bonaccurso, E.; Franz, V.; Butt, H. J., Confined liquid: Simultaneous observation of a molecularly layered structure and hydrodynamic slip. *Journal of Chemical Physics* **2002,** 117, (22), 10311-10314.

66. Schnell, E., Slippage of Water over Nonwettable Surfaces. *Journal of Applied Physics* **1956,** 27, (10), 1149-1152.

67. Cheng, J. T.; Giordano, N., Fluid flow through nanometer-scale channels. *Physical Review E* **2002,** 65, (3).

68. Ferrante, F.; Kipling, A. L.; Thompson, M., Molecular Slip at the Solid-Liquid Interface of an Acoustic-Wave Sensor. *Journal of Applied Physics* **1994,** 76, (6), 3448-3462.

69. Ellis, J. S.; McHale, G.; Hayward, G. L.; Thompson, M., Contact angle-based predictive model for slip at the solid-liquid interface of a transverse-shear mode acoustic wave device. *Journal of Applied Physics* **2003,** 94, (9), 6201-6207.

70. Du, B. Y.; Goubaidoulline, E.; Johannsmann, D., Effects of laterally heterogeneous slip on the resonance properties of quartz crystals immersed in liquids. *Langmuir* **2004,** 20, (24), 10617-10624.

71. Lauga, E.; Stone, H. A., Effective slip in pressure-driven Stokes flow. *Journal of Fluid Mechanics* **2003,** 489, 55-77.

72. Hyväluoma, J.; Kunert, C.; Harting, J., Simulations of slip flow on nanobubble-laden surfaces. *Journal of Physics-Condensed Matter* **2011,** 23, (18).

73. Steinberger, A.; Cottin-Bizonne, C.; Kleimann, P.; Charlaix, E., High friction on a bubble mattress. *Nature Materials* **2007,** 6, (9), 665-668.

74. Kunz, W.; Henle, J.; Ninham, B. W., 'Zur Lehre von der Wirkung der Salze' (about the science of the effect of salts): Franz Hofmeister's historical papers. *Current Opinion in Colloid & Interface Science* **2004,** 9, (1-2), 19-37.

75. Kunz, W., Specific ion effects in colloidal and biological systems. *Current Opinion in Colloid & Interface Science* **2010,** 15, (1-2), 34-39.

76. Parsons, D. F.; Bostroem, M.; Lo Nostro, P.; Ninham, B. W., Hofmeister effects: interplay of hydration, nonelectrostatic potentials, and ion size. *Physical Chemistry Chemical Physics* **2011,** 13, (27), 12352-12367.

77. Bostrom, M.; Kunz, W.; Ninham, B. W., Hofmeister effects in surface tension of aqueous electrolyte solution. *Langmuir* **2005,** 21, (6), 2619-2623.

78. Robertson, T. B., Contributions to the theory of the mode of action of inorganic salts upon proteins in solution. *Journal of Biological Chemistry* **1911,** 9, (3), 303-326.

79. Schwierz, N.; Horinek, D.; Netz, R. R., Reversed Anionic Hofmeister Series: The interplay of Surface Charge and Surface Polarity. *Langmuir* **2010,** 26, (10), 7370-7379.

80. Kunz, W.; Lo Nostro, P.; Ninham, B. W., The present state of affairs with Hoffmeister effects. *Current Opinion in Colloid & Interface Science* **2004,** 9, (1-2), 1-18.

81. Pegram, L. M.; Record, M. T., Hofmeister salt effects on surface tension arise from partitioning of anions and cations between bulk water and the air-water interface. *Journal of Physical Chemistry B* **2007,** 111, (19), 5411-5417.

82. Mirow, B., *Physik-Formeln*. 8 ed.; Ferd. Dümmlers Verlag: 1984.

83. Bobrinskaya, E. V.; Morozova, N. B.; Vvedenskii, A. V., Effect of alloy formation in Ag-Au system on electrical double layer structure and hydrogen evolution kinetics. *Protection of Metals* **2000,** 36, (3), 217-224.

84. Schmickler, W., *Grundlagen der Elektrochemie*. Vieweg & Sohn: Braunschweig, Wiesbaden, 1996; p. 114-120.

85. Trasatti, S., Work Function, Electronegativity, and Electrochemical Behavior of Metals: 3. Electrolytic Hydrogen Evolution in Acid Solutions. *Journal of Electroanalytical Chemistry* **1972,** 39, (1), 163-184.

86. *Landolt-Börnstein Zahlenwerte und Funktionen aus Physik, Chemie, Astronomie, Geophysik und Technik*. Springer: Berlin, Göttingen, Heidelberg, 1960; Vol. 6.

87. Parsons, D. F.; Ninham, B. W., Ab Initio Molar Volumes and Gaussian Radii. *Journal of Physical Chemistry A* **2009,** 113, (6), 1141-1150.

88. Bronstein, I. N.; Semendjajew, K. A.; Musiol, G.; Mühlig, H., *Taschenbuch der Mathematik*. 6 ed.; Harri Deutsch: 2006.

8 List of Chemicals

Name	Grade	Supplier
Ammonium nitrate(NH_4NO_3)	99+ %	Acros Organics
Cetyl trimethylammonium bromide (CTAB, structure see Figure 21)	99+ %	Acros Organics
Hydrogen peroxide (H_2O_2)	35 %	Evonik Degussa
Lutensol AT50 (structure see Figure 21)	†	BASF
Potassium chloride (KCl)	99.5+ %	Sigma-Aldrich
Potassium nitrate (KNO_3)	99 %	Riedel de Haën
Sodium acetate ($NaC_2H_3O_2$)	99 %	Sigma-Aldrich
Sodium carbonate (Na_2CO_3)	99+ %	Sigma-Aldrich
Sodium chloride (NaCl)	99+ %	Aldrich
Sodium citrate ($Na_3C_6H_5O_7$)	99+ %	Fluka Analytical
Sodium nitrate ($NaNO_3$)	99+ %	Acros Organics
Sodium perchloride ($NaClO_4$)	99+ %	Acros Organics
Sodium sulfate (Na_2SO_4)	99+ %	Merck
Sodium tartrate ($Na_2C_4H_4O_6$)	99+ %	Sigma-Aldrich
Sulfuric acid (H_2SO_4)	98 %	BASF
Tergitol MIN FOAM 1X (structure see Figure 21)	†	Dow

†: For the two commercial surfactants no grade was given by the supplier. Tergitol is a formulation hence no purity can be named and Lutensol exhibits a distribution of the molar mass.

9 Symbols and Constants

$\langle \sigma_{area} \rangle$	area averaged stress
$\langle x \rangle$	average value
a_{H+}	activity of protons
b_s	slip length
$b_{s,\,ac}$	acoustic slip length
D	dissipation
d_f	thickness of a layer with reduced viscosity
f	frequency
F	Faraday constant (96485 C/mol)
f_F	fundamental frequency
I	electrical current
m_f	mass of film per unit area
n	overtone order
N	number of values
r	bubble radius, radius of curvature
R	gas constant (8.314 J/K·mol)
r_{crit}	critical radius
s	standard deviation
T	absolute temperature
U	voltage
$\dot{u}$	velocity
u_0	amplitude of oscillation
x_i	i^{th} value of the quantity x
z	number of charges
Z_L	load impedance
Z_q	acoustic impedance of the quartz ($8.84 \cdot 10^6$ kg·m^{-2}·s^{-1})
$\Delta(\Delta p_{Laplace})$	change in Laplace pressure
Δd	film thickness
ΔD	change in dissipation
Δf	frequency shift
$\Delta p_{Laplace}$	Laplace pressure
$\Delta\Gamma$	bandwidth shift
Γ	bandwidth

δ	decay length
γ	surface tension
η	viscosity
η_f	viscosity of the film
η_L	viscosity of the liquid
φ	decomposition potential
φ_0	standard potential
π	pi (3,1416…)
θ	shear angle
ρ_f	density of the film
ρ_L	density of the liquid
σ	shear stress
σ_{vis}	viscous shear stress
$\omega = 2\pi f$	angular frequency
ζ	correlation coefficient

10 Abbreviations

AFM	Atomic Force Microscope
CE	counter electrode
CTAB	cetyl trimethylammonium bromide
CV	cyclic voltammetry
e.g.	for example
eq.	equation
EQCM	electrochemical Quartz Crystal Microbalance
FEM	Finite Element Method
FRAP	fluorescent recovery after photobleaching
QCM	Quartz Crystal Microbalance
RE	reference electrode
ref.	reference
SCE	saturated calomel electrode
SHE	standard hydrogen electrode
SLA	Small Load Approximation
vs.	versus
WE	working electrode